32nd AIAA Fluid Dynamics Conference and Exhibit
24-26 June 2002, St. Louis, Missouri

AIAA 2002-2849

RECEPTIVITY AND LINEAR STABILITY OF STETSON'S MACH 8 BLUNT CONE STABILITY EXPERIMENTS

Xiaolin Zhong * and Yanbao Ma †
University of California, Los Angeles, California 90095

ABSTRACT

Currently, the mechanisms leading to hypersonic boundary layer transition are still poorly understood. The transition in the boundary layer depends on the receptivity process, which is the process of environmental disturbances initially entering the boundary layers and generating disturbance waves. The receptivity of hypersonic boundary layers to free stream disturbances is altered considerably by the presence of bow shocks in hypersonic flow fields and by the entropy layers created by the blunt nose. This paper conducts a numerical simulation study of the receptivity to freestream acoustic disturbance waves for Mach 7.99 axisymmetric flow over a 7° half-angle blunt cone, and compares the numerical results with experimental results by Stetson et al. (1984) and with those obtained from linear stability. Both steady and unsteady flow solutions of the receptivity problem are obtained by computing the full Navier-Stokes equations using a high-order accurate shock-fitting finite difference scheme, which can accurately account for the effects of bow-shock/free-stream-sound interactions on the receptivity process. In addition, a normal-mode linear stability analysis is also used to study the stability and receptivity properties of the boundary layer affected by the entropy layer. The main focus of this study is on the excitation of the second mode waves in the receptivity process in the presense of freestream acoustic waves. One of the major findings of this study is that, for the case of receptivity to fast freestream acoustic waves with a blunt nose, the second mode waves are not excited in the early region dong the cone surface where the second modes are predicted to be unstable by the linear stability analysis. It is shown that the delay of the second mode excitation is due to the unique stability characteristics of the current flow which are affected by the entropy layer produced by the nose bluntness. The understanding of such receptivity processes may lead to a better understanding of nose bluntness effects on hypersonic boundary layer transition and the accuracy of the LST analysis.

'Professor, Mechanical and Aerospace Engineering Department, e-mail: xiaolin@seas.ucla.edu,Associate Fellow AIAA.
† Graduate Student, Student Member AIAA

INTRODUCTION

The prediction of laminar-turbulent transition in hypersonic boundary layers is a critical part of the aerodynamic design and control of hypersonic vehicles. Despite extensive studies over several decades, the mechanisms of hypersonic boundary layer stability and transition are still not well understood. Most of our knowledge of hypersonic boundary layer stability is obtained by the linear stability theory (LST)[1]. Mack was the first to find that there are higher acoustic instability modes in addition to the first-mode instability waves in supersonic and hypersonic boundary layers. Among them, the second mode becomes the dominant instability for hypersonic boundary layers at Mach numbers larger than about 4. The existence and dominance of the second mode has been observed by experimental studies [2,3].

The popular e" method for boundary layer transition prediction is based on the results of the LST analysis with an assumption that the transition is a result of the exponential growth of the most unstable normal mode waves, which are the second mode waves for hypersonic boundary layers. The criteria used in the e" method are established based on the total ratio of amplitude growth of the most unstable mode computed by the normal-mode linear stability analysis. However, the generation of the unstable mode and its initial amplitudes, which is the subject of a receptivity study, are not considered in the LST and e" method. The initial amplitudes of the most unstable mode can have a strong effect on the transition prediction from the e" method. Therefore, it is important to understand the mechanisms and characteristics of the receptivity process in hypersonic boundary boundary layers.

Practical hypersonic vehicles have blunt noses in order to reduce thermal loads. It has been generally recognized that the bow shock in front of a blunt nose has strong effects on the stability and transition of the boundary layer behind it (Reshotko 1991). Reshotko and Khan (1980) showed that the swallowing of the entropy layer by a boundary layer has a strong effect on the boundary-layer stability. The effects of nose bluntness and the entropy layer swallowing on hypersonic boundary layer transition have been studied in experiments (Potter & Whitfield 1962). The development of the second modes is strongly affected by the entropy layer in the mean flow. Overall, it has been found in

stability and transition experiments that slightly blunting the nose of a cone can greatly stablize the flow in the boundary layer.

Stetson et al. [4] carried out boundary layer stability experiments for an axisymmetric blunt cone at Mach 7.99 (Fig. 1). The half angle of the cone is 7° and the freestream Reynolds number based on the nose radius is about 33,449. The total length of the cone is about 270 nose radii, corresponding to a Reynolds number of about 9 millions. The experiments measure detailed frequency spectra of the disturbance waves along the body surface. The instability waves were found to be dominated by second mode instability. There are also significant harmonic components of the second modes. They also found evidence of entropy layer instability in the region outside of the boundary layers for the case of a blunt cone with large nose radius. This particular experiment has been identified by NATO RTO Working Group 10 on Boundary Layer Transition [5] as one of the best available stability experiments for CFD code validation. Stability experiments of hypersonic flow over similar geometries have also been done by other authors. Demetriades [6,7] did extensive stability experiments on hypersonic boundary layers over axisymmetric cones. He also presented detailed disturbance spectra in the boundary layer and obtained visualization of the laminar rope waves, which are the signature of the second mode waves in the boundary layer.

Maslov and his colleagues [8,9] reported their recent stability experiments on high speed flow. One of the test cases has similar geometry and flow conditions as those considered in Stetson's 7° blunt cone case. They being Mach 5.92 flow over a 7°-half-angle blunt cone. They also measured the frequency spectra of the disturbance waves in the boundary layer for test cases of instability waves induced both by natural disturbances in the wind tunnel and by artificial disturbances introduced into the boundary layer by high-frequency glow discharge. They found that the amplitudes of the second mode disturbances in the blunt cone boundary layer are essentially smaller than those in a sharp cone. Specifically, they found that in the case of a sharp cone, the disturbance waves in the boundary layer at the measurement location are dominated by the second mode waves. On the other hand, in the case of the blunt cone, there is a dramatic difference between the disturbance spectra obtained for flow over the blunt and sharp cones. On the blunt cone the first mode disturbances have smaller amplitudes and the second mode disturbances are practically absent. They also found that when the disturbances are induced by artificial disturbances, the amplification of the disturbances is similar for both the blunt and the sharp cones for the second mode. They conjectured that the considerable difference in the case of natural disturbances is caused by different receptivity conditions and by the development of the disturbances at low Reynolds numbers on the sharp and blunt cones.

The normal-mode stability characteristics of the boundary layer flow over the blunt cone corresponding to Stetson's experiments have been studied by three groups over the years by using linear stability analyses [10–13]. Malik et al. [10] computed the neutral stability curves and compared the growth rates with experimental results for the blunt cone case. The steady base flow solutions are computed by using parabolized Navier-Stokes equations. They found that the effect of nose bluntness is to stabilize the flow. They also compared the growth rates of LST with Stetson's experimental results at $s/R = 175$ surface station. The linear stability analyses predicted slightly lower frequency of the dominant second mode, but much higher amplification rates than the experimental results at a downstream location of 175 nose radius. Esfanhanian and Herbert [11] did similar base flow and LST calculations for the same flow by using a very fine grid resolution. They only computed and compared the growth rates at the $s/R = 175$ surface station. Similarly, Kufner et al. [12,13] also did extensive LST calculations for the same Mach 7.99 flow over the blunt cone. All three sets of LST results consistently have much larger growth rates than those of the stability experiments at 175 surface station. A comparison also shows that there are only small variations in the growth rates obtained by the different authors, with slightly different mean flow solutions. It has been speculated that the discrepancy between the linear stability results and the experimental results are due to the fact that there are significant harmonic components at the 175 nose radius station in the experimental results. The harmonics are the result of nonlinear interaction among the second modes. The nonlinear effects are neglected in a linear stability analysis. Furthermore, the effects of bow shocks, entropy layers, and non-parallel boundary layers are neglected in a normal mode stability analysis. The receptivity process, which becomes very complex due to hypersonic bow shock interaction [14,15], is not considered in the linear stability analysis. All these effects can be taken into account in a direct numerical simulation of the full Navier-Stokes equations.

Currently, direct numerical simulations have gradually become a powerful research tool in studying hypersonic boundary receptivity, stability and transition. All the effects, which are neglected by the linear stability calculations, can be taken into account in a direct numerical simulation of the full Navier-Stokes equations. The direct numerical simulation of hypersonic and supersonic boundary layer receptivity have been studied in our previous papers [16,17].

Zhong [16,18] did a numerical simulation study on the generation of boundary layer disturbance waves due to free stream waves, for a two-dimensional Mach 15 viscous flow over a parabola. Both steady and unsteady flow solutions of the receptivity problem are obtained by computing the full Navier-Stokes equations

using a high-order accurate shock-fitting finite difference scheme. The effects of bow-shock/free-stream-sound interactions on the receptivity process are accurately taken into account by treating the shock as a discontinuity surface, governed by the Rankine-Hugoniot relations. The results show that the disturbance waves generated and developed in the hypersonic boundary layer contain both the first, second, and third mode waves. A parametric study is carried out on the receptivity characteristics affected by different free-stream waves, frequencies, nose bluntness characterized by Strouhal numbers, Reynolds numbers, Mach numbers, and wall cooling. It is found that the receptivity parameters decrease when the forcing frequencies or nose bluntness increase.

Ma and Zhong [17], studied the mechanisms of the receptivity of supersonic boundary layer to freestream disturbances by using both direct numerical simulation and linear stability theory. Specifically, the receptivity of a Mach 4.5 flow over a flat plate to freestream fast acoustic waves is studied. The results show that the receptivity of the flat plate boundary layer to freestream fast acoustic waves leads to the excitation of both Mack modes and a family of stable modes, i.e., mode I, mode II, etc. It is found that the forcing fast acoustic waves do not interact directly with the unstable Mack modes. Instead, the stable mode I waves play an important role in the receptivity process because they interact with both the forcing acoustic waves and the unstable Mack-mode waves. Through the interactions, the stable mode I waves transfer wave energy from the forcing fast acoustic waves to the second Mack-mode waves. The effects of incident wave angles, forcing wave frequencies, and wall temperature perturbation conditions on the receptivity are studied. The results show that the receptivity mechanisms of the second mode are very different from those of mode I and mode II, which lead to very different receptivity properties of these discrete wave modes to freestream fast acoustic waves with different incident wave angles, frequencies, and different wall boundary conditions.

Because the issue of hypersonic boundary layer stability involves many complex mechanisms, it is necessary to conduct validation studies by comparing numerical simulation results with those of stability experiments. The CFD code validation on hypersonic boundary layer transition is one of the subjects of the NATO RTO Working Group 10 [5]. The Mach 7.99, 7° blunt cone of Stetson's experiment is identified by the NATO Working Group as one of the best available stability experiments for code validation. Schneider [5] also presented some of Stetson's results which were not published before and did some LST calculations. In addition, the test case of Stetson's blunt cone experiments is also a very good case for studying the receptivity and stability of the boundary layer affected by the nose bluntness and entropy effects. The DNS studies can also shed light on the effectiveness and accuracy of the LST analyses for hypersonic boundary layers.

Therefore, we [19] have been conducting the numerical simulation of Stetson's 7° blunt cone in Mach 7.99 flow for two purposes: 1) to compare numerical results with the experimental results, and 2) more importantly, to study the detailed receptivity and stability mechanism by numerical simulations. In a previous paper [19], we have done one case of initial stability calculations with seven frequency components in the forcing waves in surface blowing and suction. The results showed that the wave modes develop into second-mode waves downstream. The dominant wave frequencies agree well with experimental results. The eigenfunction of the modes obtained by the numerical simulations also agree very well with the LST results. The numerical results also show the development of second harmonics due to the nonlinear interaction among these fundamental waves. The receptivity process has not been studied.

The objective of this paper is to study the receptivity to freestream acoustic waves of the 7° half-angle blunt cone in Mach 7.99 flow, corresponding to the stability experiment by Stetson et al. [4] The numerical simulation of the full nonlinear Navier-Stokes equations are able to take in to account the nonlinear wave interactions, the bow shock and entropy layer effects, the wall curvature effects, and the non-parallel mean flow effects on the stability of the boundary layer. The particular test case studied in tbis paper is a Mach 7.99 axisymmetric flow over a blunt circular cone with nose radius of 0.15 inch at zero angle of attack. Both steady and unsteady flow fields between the bow shock and the boundary layer are numerically simulated by using a high-order shock-fitting scheme to study the wave generation in the boundary layer. Whenever possible, the results are compared with experimental results. In addition, an axisymmetric LST code has also been developed to study the linear stability and receptivity properties of the boundary layers. The LST results are also used to identify and analyze the simulation results. Using the comparison of simulation results and experimental results, we would like to gain a better understanding of the hypersonic boundary layer instability mechanism.

GOVERNING EQUATIONS AND NUMERICAL METHODS

The stability of axisymmetric laminar hypersonic flow over a blunt cone at zero angle of attack is computed using a three-dimensional grid. The governing equations are briefly presented in this section. Details can be found in previous papers for 2-D and 3-D flows [18,20]. The governing equations are the unsteady full three-dimensional Navier-Stokes equations written for the computation in the conservation-law form:

$$\frac{\partial U^*}{\partial t^*} + \frac{\partial F^*_j}{\partial x^*_j} + \frac{\partial F^*_{vj}}{\partial x^*_j} = 0 \qquad (1)$$

where superscript "*" represents dimensional variables, and

$$U^* = \{\rho^*, \rho^* u_1^*, \rho^* u_2^*, \rho^* u_3^*, e^*\}. \quad (2)$$

The equations of states are $p^* = \rho^* R^* T^*$ and $e^* = \rho^*(c_v^* T^* + \frac{1}{2} u_k^* u_k^*)$, where the gas constant R^* and the specific heats c_p^* and c_v^* are assumed to be constants. The flux vectors in Eq. (1) are

$$F^*_j = \begin{Bmatrix} \rho^* u_j^* \\ \rho^* u_1^* u_j^* + p^* \delta_{1j} \\ \rho^* u_2^* u_j^* + p^* \delta_{2j} \\ \rho^* u_3^* u_j^* + p^* \delta_{3j} \\ (e^* + p^*) u_j^* \end{Bmatrix} \quad (3)$$

$$F^*_{vj} = \begin{Bmatrix} 0 \\ -\tau_{1j}^* \\ -\tau_{2j}^* \\ -\tau_{3j}^* \\ -\tau_{jk}^* u_k^* - q_j^* \end{Bmatrix} \quad (4)$$

where τ_{ij}^* is the viscous stress tensor and q_j^* is heat flux vector. The gas is assumed to be thermally and calorically perfect. The viscosity and heat conductivity coefficients are calculated using Sutherland's law together with a constant Prandtl number, Pr. The equations are transformed into body-fitted curvilinear computational coordinates in a computational domain bounded by the bow shock and the body surface. The location and the movement of the bow shock is an unknown to be solved for along with the flow variables by a shock-fitting method described in [21]. The numerical simulation for the axisymmetric hypersonic flow over a blunt cone is carried out using our 3-D fifth-order shock fitting scheme where the outer grid line is the bow shock. The unsteady bow shock shape and shock oscillations are solved as part of the computational solution. The numerical methods for spatial discretization of the 3-D full Navier-Stokes equations are a fifth-order shock-fitting scheme in streamwise and wall-normal directions, and a Fourier collocation method in the periodic spanwise flow direction for the case of a wedge geometry or in the azimuthal direction for the case of a cone geometry. The spatially discretized equations are advanced in time using a Runge-Kutta scheme of up to third order. The numerical methods and computer code have been extensive validated and tested in many 2-D and 3-D viscous flow simulations discussed in our previous papers (for example, [21]). The validation results are not presented in this paper.

Because the flow field behind the bow shock is not uniform, the flow variables are nondimensionalized using the freestream conditions as characteristic variables. Specifically, we nondimensionalize the velocities with respect to the freestream velocity U_∞^*, length scales with respect to the nose radius r^*, density with respect to ρ_∞^*, pressure with respect to p_∞^*, temperature with respect to T_∞^*, time with respect to r^*/U_∞^*, vorticity with respect to U_∞^*/r^*, entropy with respect to c_p^*, wave number by $1/r^*$, etc. The dimensionless flow variables are denoted by the same dimensional notation but without the superscript "*".

FLOW CONDITIONS

The flow conditions are the same as Stetson's experiments on a blunt cone, i.e.,

$M_\infty = 7.99$
$p_t^* = 4 \times 10^6$ Pa $\qquad T_t^* = 750\ K$
$\gamma = 1.4 \qquad Pr = 0.72$
$Re_\infty = \rho_\infty^* U_\infty^* r_n^* / \mu_\infty^* = 33,449$

The viscosity is computed using the Sutherland's law for air. The cone is a 7° half angle blunt cone with a spherical nose of radius: $r_n^* = 3.81 \times 10^{-3}\ m$. The total length of the cone is $L = 1.016\ m$. The corresponding Reynolds number at this length is $Re_L = 8.92 \times 10^6$. The body surface is assumed to be a non-slip wall with either an isothermal wall with temperature T_w^* or an adiabatic wall.

The wall surface in the experiment was neither isothermal nor adiabatic. In order to access the effects of wall temperatures on the boundary-layer stability properties, a number of cases with different isothermal wall temperatures and a case of adiabatic wall are considered. So far, we have finished two cases:

1. An isothermal wall with a constant wall temperature of $T_w^* = 800\ K$,
2. An adiabatic wall.

Since the previous LST studies were mainly done for the case of adiabatic wall, we will mainly present the results for the case of adiabatic wall in this paper. The numerical solutions are compared with the experimental results published by Stetson et al. [4] and some newly compiled results by Schneider [5]. For steady flow solutions, the current Navier-Stokes solutions are also compared with the solutions of the thin-layer Navier-Stokes equations by Esfahanian and Herbert [11,22].

The main objective of this paper is to study the receptivity of the second modes and and their harmonics. In stability experiments by Stetson et al. [4], the instability waves in the boundary layer were generated naturally in a relatively noisy wind tunnel without artificial forcing disturbances. Stetson et al. [4] showed detailed frequency spectra of disturbance waves at various surface stations. Figure 2 shows the experimental fluctuation spectra along the cone surface obtained by Stetson et al. The wave spectra of this figure show clearly that the instability waves are dominated by two-dimensional second modes and their harmonics. As the observation station moves downstream, the frequency of the dominant second mode reduces and the strength of the harmonics increase. At the station of 175 nose radii,

the second mode wave is maximum at the frequency of about 135 kHz.

In order to reproduce similar flow conditions in the numerical simulations, it is necessary to introduce initial forcing waves to excite the instability waves in the boundary layer. The forcing waves can originate from the freestream or at the wall by surface roughness or vibrations. For a receptivity simulation, it is necessary to impose forcing disturbances in the free stream. In Stetson's experiments, the freestream is dominated by acoustic waves generated by the wind tunnel wall. Figure 3 shows the freestream disturbance spectra in Stetson et al.'s experiments (1984). The middle line corresponds to the current test case of freestream unit Reynolds number of 2.5×10^6 per feet. Therefore, as a first step, we simulate the stability experiment by imposing freestream acoustic disturbances according the freestream fluctuation spectra of the experiments given by Fig. 3. In addition, we also introduce the disturbances by the blowing and suction of a narrow surface strip in the upstream region of the body surface in order to compare the growth rates of the second mode. Since the wave fields in the experiment contain a wide range of second-mode frequencies, we introduce, by surface blowing and suction, disturbances of a number of frequencies near the dominant second mode waves in the simulation. The subsequent receptivity and development of the instability waves at these frequencies and their harmonics due to nonlinear interactions are computed by the numerical simulation.

FORCING WAVE IN RECEPTIVITY SIMULATIONS

The receptivity of a axisymmetric Mach 7.99 boundary layer to free stream waves for hypersonic flows past a 7° half angle blunt cone at zero angle of attack is considered. Free stream disturbances are superimposed on a steady mean flow before reaching the bow shock, to investigate the process of free stream waves entering the boundary layer and inducing boundary-layer waves. As a first step, the free stream disturbances are assumed to be weak planar fast acoustic waves with wave fronts normal to the center line of the body. Other forms of freestream disturbances, especially slow acoustic waves and 3-D waves, will be studied in a future paper.

Specifically, we impose simultaneously N independent 2-D planar fast acoustic waves of different frequencies in the freestream. The amplitudes of each wave frequency is proportional to the wind tunnel spectra shown in Fig. 3. The wave fields are represented by the perturbations of instantaneous flow variables with respect to the local steady base flow variables at the same location. For example, instantaneous velocity perturbation u' located at (x, y), at time t, is defined as:

$$u'(x,y,t) = u(x,y,t) - U(x,y) \qquad (5)$$

where $u(x,y,t)$ is the instantaneous velocity component obtained by an unsteady numerical simulation of the nonlinear Navier-Stokes equations, $U(x,y)$ is the steady mean flow velocity obtained by a separate steady flow simulation. For weak acoustic waves in the free stream before reaching the bow shock, we impose a acoustic waves with a total of N frequencies, i.e., the perturbation of an arbitrary flow variable can be written in the following form:

$$q_\infty(x,y,t)' = |q'| \sum_n^N A_j \, e^{i[n\,\omega_1(\frac{x}{c_\infty}-t)+\phi_n]} \qquad (6)$$

where $|q'|A_n$ represents the wave amplitude of the freestream perturbation of any flow variables at a frequency

$$\omega_n = n\,\omega_1 \qquad (n = 1, 2, \cdots, N) \qquad (7)$$

where ω_1 is the minimum frequency of the waves. The relative amplitude of each ω_n frequency, $A_n > 0$ is determined by Fig. 3 such that,

$$\sum_n^N A_n^2 = 1 \qquad (8)$$

In the equation above, c_∞ is the wave speed in the free stream before reaching the shock. The initial phase angle, ϕ_n, of the forcing acoustic wave at frequency ω_n is determined randomly. The absolute amplitude of the wave group is determined by setting the values of $|q'|$. For fast acoustic waves in the freestream, perturbation amplitudes of nondimensional flow variables satisfy the following dispersion relations:

Fast Acoustic Waves:

$$c^*_\infty = u^*_\infty + a\&$$
$$|\rho'|_\infty = |p'|_\infty/\gamma = |u'|_\infty M_\infty = \epsilon M_\infty;$$
$$|s'|_\infty = |v'|_\infty = 0$$

where ϵ is a small number representing the relative amplitude of the group of free stream acoustic waves. The forcing disturbances contain N wave frequencies which are multiples of ω_1, which are chosen such that the frequencies cover the dominant second-mode frequencies observed in the experiment.

The flow is characterized by a free stream Mach number $M_\infty = \frac{u^*_\infty}{a^*_\infty}$, and a Reynolds number defined by $Re_\infty = \frac{\rho^*_\infty U^*_\infty d^*}{\mu^*_\infty}$. The forcing frequency of the free stream acoustic wave is represented by a dimensionless frequency F defined by

$$F = 10^6 \frac{\omega^* \nu^*}{U^{*2}_\infty} = 10^6 \, \omega / Re_\infty \qquad (9)$$

where F represents the wave frequency with respect to a viscous flow scale. We can also define a Strouhal number S using the nose radius by

(10)

where r^* is the nose radius. The Strouhal number represents the relative nose bluntness in the receptivity problem.

In addition, we also introduce the disturbances by blowing and suction in a narrow surface strip in the upstream region of the body surface. Since the wave fields in the experiment contain a wide range of second-mode frequencies, we introduce, by surface blowing and suction, disturbances of a number of frequencies near the dominant second mode waves in the simulation. The subsequent receptivity and development of the instability waves at these frequencies and their harmonics due to nonlinear interactions are computed by the numerical simulation. The purpose of such studies is to study the excitation and generation of the second mode in the boundary layer. The specific formulas for surface blowing and suction in a narrow upstream range are given by the perturbations to the wall normal velocity, i.e.,

$$v_n(x,t) = \epsilon \sin[\alpha_w(x - x_0)] \sum_{n=0}^{N} A_n \cos(n\omega_0 t + \phi_n) \qquad (11)$$

$$(x_0 \le x \le x_1)$$

where ϵ is a small nondimensional number representing forcing disturbance amplitudes. The forcing disturbances contain a number of wave frequencies which are multiples of ω_0, which are chosen such that the frequencies cover the dominant second-mode frequencies observed in the experiment. Nonlinear wave interactions can be studied by increasing the amplitudes of the forcing waves. This can be achieved by increasing the value of ϵ.

The numerical simulation for an unsteady hypersonic layer stability problem is carried out in two steps. First, a steady flow field is computed by advancing the unsteady flow solutions to convergence with no disturbances imposed. Second, unsteady viscous flows are computed by imposing freestream waves given by Eq. (6), or by imposing surface blowing-and-suction at the narrow surface strip in addition to the steady flow variables according to Eq. (11).

LINEAR STABILITY ANALYSIS FOR AXISYMMETRIC FLOWS

The instability of hypersonic boundary layer flow over the Stetson's 7° half-angle blunt cone has been studied extensively [10–13] by using the normal-mode linear stability theory. However, previous LST studies have been mainly focused on the instability of the most unstable first and second-mode waves. In our previous receptivity study of Mach 4.5 boundary layer flow [17], it was found that a family of other wave modes, which are stable in a linear stability analysis, play an important role in the receptivity process. They are termed mode I, II, III, etc. in [17]. The stable wave modes generated by the forcing waves through resonant interactions can interact with the instability waves once they are generated. In order to understand the receptivity process, it is necessary to understand the characteristics of these stable wave modes, in addition to the Mack modes. The characteristics of these stable wave modes in hypersonic flows with nose bluntness have not been studied. Therefore, we will use the LST approach to study the wave mode properties of mode I, mode II, etc. in addition to those of the first and second Mack modes. In addition, the LST analysis is used to identify and analyze the boundary layer eigenmodes generated by forcing disturbances in the numerical simulations. Therefore, the characteristics of normal modes of the axisymmetric hypersonic boundary layer are studied by the linear stability theory in this paper.

In the studies of boundary-layer stability, the following Reynolds number, R, based on the length scale of boundary-layer thickness is often used:

$$R = \frac{\rho_\infty^* u_\infty^* L^*}{\mu_\infty^*} \qquad (12)$$

where length scale of boundary-layer thickness is defined as

$$L^* = \sqrt{\frac{\mu_\infty^* s^*}{\rho_\infty^* u_\infty^*}} \qquad (13)$$

where s^* is the curvature length along the wall surface measuring from the leading edge. Hence, the relation between R and local Reynolds number Re_s is

$$R = \sqrt{Re_s}\,. \qquad (14)$$

Formulation of Linear Stability Analysis

The flow disturbances in the boundary layers of axisymmetric flows are represented by the perturbations of instantaneous flow variables with respect to their local base flow solutions. For example, the instantaneous velocity perturbation u' is defined as the linear perturbation with respect to the local base velocity, i.e.,

$$u'(x,y,4,t) = u(x,y,\phi,t) - \bar{u}(x,y) \qquad (15)$$

where $\bar{u}(x,y)$ is the base flow velocity. In general, instantaneous flow variables can be written in the following form,

$$q = \bar{q} + q' \qquad (16)$$

where q stands for u, v, w, p, ρ, or T. The linear stability theory is based on the normal mode analysis under a parallel flow assumption. Specifically, the linear fluctuations of flow variables are decomposed into a normal mode form as follows

$$q' = \hat{q}(y_n)\, e^{i(-\omega t + \alpha s)} \qquad (17)$$

where $\hat{q}(y_n)$ is the complex amplitude of the disturbances, n and s are the coordinates along the wall-normal and surface directions respectively, $a = \alpha_r + i\alpha_i$, is the streamwise complex wave number, and w is the circular frequency. Under the parallel flow assumption, the linearized governing equations in an axisymmetric flow of $\hat{q}$ in Eq. (17) can be expressed as

$$(\mathbf{A_0}\frac{d^2}{dy_n^2} + \mathbf{B_0}\frac{d}{dy_n} + \mathbf{C_0})\,\hat{q} = 0\,, \qquad (18)$$

where matrices A_0, B_0, and C_0 are functions of α, w, R, and the profiles of the steady axisymmetric base flow variables. The detailed formulas for these matrices can be found in [22]. A non-slip condition is used for velocity perturbations at the wall. The temperature perturbation condition at the wall is either the isothermal or the adiabatic condition. The boundary-layer disturbances are assumed to decay exponentially as y_n approaches ∞. The specific boundary conditions used in LST calculations are

$$\hat{u} = \hat{v} = \hat{w} = 0\,, \quad \hat{T} = 0 \text{ or } \frac{d\hat{T}}{dy_n} = 0 \text{ at } y_n = 0\,;$$
$$\hat{u}, \hat{v}, \hat{w}, \hat{T} \to 0 \quad \text{as } y_n \to \infty\,. \qquad (19)$$

It should be noted that both the adiabatic wall and the isothermal wall boundary condition for temperature perturbations can be used to close the governing equations. The homogeneous governing equations (18) with boundary conditions given by Eqs. (19) lead to an eigenvalue problem. In a spatial linear stability analysis, complex parameter a and complex function $\hat{q}(y)$ are obtained as the eigenvalues and the eigenfunctions of the stability equations for a given frequency w. For the spatial problem, w is real, and α is a complex wave number where a, and α_i represent the spatial wave number and growth rate of a wave mode respectively. A linear wave mode is unstable when α_i is negative for the spatial problem.

Axisymmetric LST Code Validation

A LST computer code based on multi-domain spectral method of Malik [23] is developed. Before we carry out the linear stability theory to identify instability modes, the LST code is validated and compared with experimental results and other published LST results.

Figure 4 compares spatial growth rates for Mach 7.99 7° half-angle blunt cone with adiabatic wall for base flow at surface station $s/r = 175$. Both adiabatic and isothermal wall boundary conditions for wall temperature perturbations are considered in the current study. The experimental results of Stetson and other LST results are also plotted in the same figure for comparison. This figure shows that higher growth rates are obtained for an adiabatic wall compared with an isothermal wall boundary condition. The figure also shows that our results associated with an isothermal wall boundary condition compare well with other LST results that use the same wall boundary conditions. The differences between the current LST results and those of other authors are mainly due to different mean flow solutions used by different LST computations. Again, the linear stability theory predicts much higher growth rates than the experiments do. Since the DNS simulations of the current paper involve minimum simplifications in the flow model, the growth rates predicted by full Navier-Stokes simulation are expected to shed light on the reason for the difference in growth rates predicted by LST and those observed in experiments. Figure 4 also shows that at the surface location of 175 nose radii, the second mode instability range is in the range between 100 kHz and 170 kHz. The first mode unstable frequency range is lower than 100 kHz.

Besides the eigenvalues, eigenfunctions of the second mode at the same station for w = 0.1934 (127.56 kHz) are also compared with Esfahanian and Herbert's [22] LST results, which are plotted in figure 5. It shows that there is an excellent agreement in the second-mode profiles of temperature perturbations. Such agreement is also obtained in the comparison of eigenfunctions for other variables, which is not shown here. Therefore, the LST code for axisymmetric boundary layer flows is accurate. These comparisons of eigenvalues and eigenfunctions with other published LST results show the correctness of the LST results obtained by the current LST code used in this paper.

The grid resolution required for accurate LST calculations is investigated by grid refinement studies. Figure 6 compares results obtained by using two sets of grids, for the real and imaginary part of T eigenfunctions of the second mode from the linear stability theory at the $s/r = 175$ surface location for the frequency of 127.56 kHz. The two sets of grids are 100 and 200 points across the boundary layer respectively. The two sets of results are almost identical to each other. Therefore, the grid resolution of 100 grid points is used in the current study. This grid size is enough for good resolution of the problem.

STEADY BASE FLOW SOLUTIONS

The steady base flow solutions of the Navier-Stokes equations for the axisymmetric Mach 7.99 flow over the blunt cone are obtained first by advancing the solutions to a steady state without forcing waves. The simulation is carried out by using a multi-zone approach using 28 zones with a total of 3360 by 121 grid points for the axisymmetric flow field from the leading edge to the 190 nose radius surface station. The corresponding Reynolds number at the 190 nose radius surface station is 6.36×10^6. The results presented in this paper are those for the case of adiabatic wall only. Some results for the ease of isothermal wall at $T_w^* = 800K$ have been

presented in a previous paper [19].

Results Comparisons and Validation

Esfahanian and Herbert [11,22] performed highly accurate mean flow calculations of the same flow field using the thin-layer Navier-Stokes equations and a fine grid of 1300 by 100 points. The shock is also computed by a shock-fitting scheme. They compared some of their mean flow solutions with the available experimental results of Stetson. In this paper, we compared our results with those of Esfahanian and Herbert [11,22] and the experimental results. It should be pointed out that the full Navier-Stokes equations are used in the current study, while Esfahanian and Herbert used the thin-layer approximation of the Navier-Stokes equations. Though the differences between the two sets of equations should be very small in the downstream region, it is expected that there may be some noticeable differences in the two results in the region near the stagnation streamline, where the thin-layer approximation used in Esfahanian and Herbert's studies may not be accurate.

Figure 7 shows the Mach number contours of the current steady state solution in about 1/3 of the computational domain near the leading edge region. In the simulation, the bow shock shape is not known in advance and is obtained as the solution for the freestream computational boundary. The results show that the Mach numbers immediately behind the bow shock approach a constant value of about 7 behind the shock at downstream locations. The locations of bow shock obtained by Esfahanian and Herbert are also marked in the same figure. The shapes of the two bow shocks agree very well. Esfahanian and Herbert also showed that their bow shock agree very well with Stetson's experiments. Therefore, the current results on the bow shape are accurate.

Figure 8 compares the steady pressure distribution along the cone surface between the current computation, the experimental results obtained by Stetson et al [4], and thin-layer Navier-Stokes results obtained by Esfahanian and Herbert. There is a discontinuity in surface curvature at the junction of the sphere nose and cone afterward. The flow experiences an overexpansion at the junction and goes through a recompression along the cone surface afterward. As a result, there is a slight adverse pressure gradient at downstream surface locations. The figure shows that the surface pressure compares very well with the experimental results and those of Esfahanian and Herbert.

Figures 9 shows the surface temperature distributions along the cone surface for the current case of adiabatic wall. The current Navier-Stokes solutions agree very well with those of Esfahanian and Herbert of the thin-layer Navier-Stokes solutions. However, both sets of independently obtained numerical solutions predict higher surface temperatures than the experimental results, which indicate that the cone surface in Stetson's experiments was not perfectly adiabatic. The actual surface temperatures are about 10 to 20% lower than those of the adiabatic wall. Therefore, it is necessary study the effects of wall temperatures on the receptivity and stability of the same flows. For the current study, only the case of adiabatic wall is considered. The parametric effects of wall temperatures, as well as other effects, will be studied in a future paper.

The tangential velocity profiles across the boundary layer at a surface location of $s/r = 94$ and 128 are shown in Figs. 10 and 11. Current Navier-Stokes results are compared with those of Esfahanian and Herbert and the experiments. The experimental measure ment could only reach to a certain distance from the wall surface because of the size limit of the experimental probes. The figures show that the current results agree with those obtained by Esfahanian and Herbert's calculations. The velocity magnitudes agree well with the experiments in the flow region outside of the boundary layer. The computed velocities inside the boundary layer are slightly larger than the experimental values. The discrepancy may be due to experimental errors or other factors. Similarly, the profiles of current pressure and temperatures at $s/r = 54$ station are also compared with those of Esfahanian and Herbert in Figs. 12 and 13. No experimental results are available in these figures. Again, current results agree very well with the thin-layer Navier-Stokes solutions obtained by Esfahanian and Herbert.

Entropy Layer

The linear stability analysis of the boundary layer is carried out using the steady profile obtained by the simulation. In the LST calculations, it is necessary to provide the first and second derivatives of velocity and temperature profiles in the wall-normal direction. Figures 14 and 15 show the distribution of the second derivatives of tangential velocities at two surface locations. The curve of the second derivatives in these figures have a strong valley near the edge of the boundary layer. However, comparing the profiles at these two stations, there is evidence that the second derivative curve at the earlier 31.9 station has a second valley outside of the boundary layer. This second valley is a result of the entropy layer created by the curved bow shock in the nose region. The entropy layer has been shown to play an important role in the stability and transition of hypersonic boundary layers. The entropy layer, which is generated at the bow shock in the nose region, gradually approaches the wall and merges with the boundary layer as it moves downstream. At further downstream locations, the entropy layer is completely "swallowed" by the boundary layer and the boundary layer approaches the same self-similar profile as that of a sharp cone. It is interesting to investigate how the

entropy layer affects the stability of the boundary layer flow over a blunt cone.

The entropy layer is examined further by comparing the steady flow solutions at different stations along the cone surface. In this paper, we mainly study the effect of the entropy layer on the parameter $\rho(du_t/dy_n)$ related to the generalized inflection point in the boundary layer. Lees and Lin [24] showed that the existence of a generalized inflection point is a necessary condition for inviscid instability in a compressible boundary layer.

Figure 16 show the contours of $\rho\frac{du_t}{dy_n}$ obtained by the current simulations. The figure shows that the peaks in the contour lines are located initially behind the bow shock and outside of the boundary layer. The peaks gradually approach the wall and merge with the boundary layer on the wall. This is a very clear indication of the creation of the entropy at the bow shock and affecting the steady base flow field. Figures 17 to 20 plot the profiles of $\rho\frac{du_t}{dy_n}$ along the wall-normal direction at four surface locations ranging from $s/r = 18.9$ near the leading edge to $s/r = 169.4$ far downstream. In the region near the leading edge, Fig. 17 shows two distinct regions in the $\rho\frac{du_t}{dy_n}$ profile with two separate peaks: one inside the boundary layer and another outside the boundary layer. The second peak is created by the entropy layer. For compressible flat plate boundary layers, Lees & Lin (1946) showed that the existence of a generalized inflection point is a necessary condition for inviscid instability. The generalized inflection point is located at $d(\rho du/dy_n)/dy = 0$. The additional peak outside of the boundary layer may be responsible for instability waves in the entropy layers. As s increases to 31.9 in Fig. 18, the two peaks gradually merge. Further downstream at $s/r = 88.3$, the peak outside of the boundary layer is totally absorbed by the boundary layer. There is only one peak in the profile. Still further downstream at $s/r = 169.4$ in Fig. 20, the profile becomes essentially the same as those without the entropy layer effects. Therefore, in the current case, the entropy layer gradually merges with the boundary layer, though it is difficult to define the precise location where the entropy layer is swallowed by the boundary layer. It is expected that the stability and receptivity characteristics will be strongly affected by the existence of the entropy layer in terms of the mean flow changes and disturbance flow due to the new generalized inflection point.

RECEPTIVITY TO FREESTREAM ACOUSTIC WAVES

Having obtained the steady solution, the receptivity of Stetson's Mach 7.99 flow over the blunt cone to freestream acoustic waves is simulated by solving the full Navier-Stokes equations. The forcing waves are free-stream planar fast acoustic waves with 15 frequencies. Boundary-layer receptivity to free-stream acoustic disturbances is studied for.axisymmetric hypersonic. flow over the 7° half-angle blunt cone. The unsteady flow solutions are obtained by imposing acoustic disturbances on the steady flow solutions in the free stream. The subsequent interaction of the disturbances with the shock and the receptivity of the boundary layer over the parabola are computed by using the full Navier-Stokes equations.

Table 1: Acoustic wave components in the freestream.

n	f_n^* (kHz)	F_n	A_n	ϕ_n (radian)
1	14.92	9.035	0.7692	2.4635(-6)
2	29.84	18.07	0.4162	0.1600
3	44.77	27.11	0.2827	2.2149
4	59.68	36.14	0.2065	4.1903
5	74.61	45.18	0.1707	6.0510
6	84.53	54.21	0.1406	5.2671
7	104.5	63.25	0.1132	2.1070
8	119.4	72.28	9.7164(-2)	5.7511
9	134.3	81.31	0.1081	5.0005
10	149.2	90.35	9.0781(-2)	5.2319
11	164.1	99.39	7.7722(-2)	2.1679
12	179.1	108.4	5.8428(-2)	5.4738
13	194.0	117.5	5.0729(-2)	0.5649
14	208.9	126.5	7.6987(-2)	5.5812
15	223.8	135.5	5.7108(-2)	4.4043

In the current test case presented in this paper, the freestream acoustic waves contain 15 frequencies with the lowest frequency of $f_1^* = 14.922kHz$ corresponding to dimensionless frequency of $F_1 = 9.04$. The effects of entropy layer and nose bluntness on the receptivity are studied by simulation of the full Navier-Stokes equations. The wave modes are identified and the growth rates and wave spectra are compared with LST analysis and eventually with Stetson's experiments. The wave amplitudes in the freestream are set according to the experimental freestream wave spectra reported by Stetson as shown in Fig. 3. The phase angles of the waves in Eq. (6) are chosen randomly. Specifically, the wave frequencies, amplitudes, and phase angles used in the current receptivity simulation are given in Table 1. The overall wave amplitude is $\varepsilon = 6.2578 \times 10^{-4}$ with 15 frequencies ($N = 15$).

The unsteady calculations are carried out until the solutions reach a periodic state in time. Temporal Fourier analysis is carried out on local perturbations of unsteady flow variables after a time periodic state has been reached. The Fourier transform for the real disturbance functions lead to:

$$q'(x,y,t) = \Re\{\sum_{n=0}^{N} |q_n(x,y)|\, e^{i[-n\omega_1 t + \phi_n(x,y)]}\} \qquad (20)$$

where $n\omega_1$ is the frequency of the n-th wave mode,

$q'(x, y, t)$ represents any perturbation variables, and $|q_n(x,y)|$ and $\phi_n(x, y)$ are real variables representing the local perturbation amplitude and phase angle of the n-th wave mode. These variables indicate the amplitude of local disturbances and the local phase angle with respect to the forcing waves in the freestream. For perturbations in the boundary layer near the body surface, we can define a local growth rate α_r and a local wave number α_i of the perturbation fields by,

$$\alpha_i = \frac{1}{|q_n|}\frac{d|q_n|}{dx} \quad (21)$$

$$\alpha_r = \frac{d\phi_n}{dx} \quad (22)$$

where the derivatives are taken along a grid line parallel to the body surface.

Although the mean flow has an adiabatic wall with a zero temperature gradient on the wall, it has been argued that the temperature perturbations should be set to zero because of the relatively high frequencies of the second mode. In our simulations, however, a wide range of frequencies are simultaneously imposed in the freestream. It is likely that the actual temperature perturbations may be some where between the two extreme of $\partial T'/\partial y_n = 0$ and $T' = 0$. Therefore, we simulate both cases of different temperature perturbations conditions on the wall with the same mean flow. It is found that the stability and receptivity characteristics are very similar for both cases. In this section, we will first present the results of the test case of $\partial T'/\partial y_n = 0$ boundary condition, followed by the results of same receptivity simulation using the $T' = 0$ boundary condition.

CASE I. $\frac{\partial T'}{\partial y_n} = 0$ BOUNDARY CONDITION

The results presented here are those for the case of zero gradient temperature perturbation boundary conditions. The steady base flow has an adiabatic wall. The unsteady flow solutions are obtained by imposing freestream disturbances according to Table 1 and Eq. (6), containing 15 frequencies.

Simulation Results

Figure 21 shows the development of wave amplitudes of pressure perturbations in the boundary layer as functions of x/r. The lines represent 15 different frequencies of $f = nf_1$, where $f_1^* = 14.922kHz$ and $n = 1, 2, \cdots, 15$. The relative amplitudes in the freestream of each frequency is set to be proportional to that given by Fig. 2 of Stetson's experiments as shown in Table 1. The figure shows the development of wave modes induced by the freestream forcing waves. However, there is no apparent presence of the unsteady second mode in the main computational region. This is an unexpected result because in the frequency range covered by the current simulation, the LST analysis has shown that the second mode is unstable starting from the region near $x/r = 90$ for frequency at 149.2kHz ($n = 10$). On the other hand, as shown in Fig. 2, Stetson's experiments also showed that the disturbances waves are not dominated by the second mode until it reaches the region much downstream at 212 surface station. Therefore, the simulation results are consistent with the experimental results shown in Fig. 2 that the second mode is not dominant in earlier surface stations. The growth rates predicted by LST are substantially higher than those obtained by experiments. The frequency of the mast unstable second mode predicted by LST is approximately in the range of 130 kHz (around n = 9 in Fig. 21). However, Fig. 21 shows that the wave amplitudes for the frequency of 134 kHZ ($n = 9$) have no clear unstable growth as it is expected for the unstable second mode. Also in Fig. 21, the disturbances of $n = 3$ and $n = 4$ are growing along the surface. But we will show later that these are not the Mack modes. They are the stable mode I waves which are induced by the forcing acoustic waves through resonant interactions.

In order to examine the development of wave amplitudes of each frequency more clearly, the wave amplitude spectra for surface presure perturbations obtained by the numerical simulation are shown in Figs. 22 to 25 for several surface stations. Figure 22 shows the frequency spectrum of the pressure perturbations on the cone surface at the surface location of 18.9 nose radii. The subsequent figures show the development of wave spectra at downstream surface locations. The frequency spectrum at the surface location of 130 nose radii, plotted in Figure 24 shows that the unstable second mode is not apparent in the numerical solutions. As the flow develops further downstream at the $s = 175.4$ station, the frequency of $n = 10$ at 149.2 kHz shows signs of initial development of unstable second mode as shown in Fig. 25.

Since there is an indication of the development of the second mode in Fig. 25, the amplitudes of pressure perturbations along the cone surface for this frequency are plotted in Fig. 26. The figure shows there are wave modulations of multiple waves as the waves propagate downstream along the surface. The figure shows that the wave amplitudes increase starting from the surface station around $x/r = 140$. However, the second mode is predicted to be unstable at this frequency starting from $x/r \approx 90$. Therefore, the excitation of the second mode does not coincide with the beginning of the unstable region predicted by LST. The development of the wave modes can also be seen from the temperature disturbance contours shown in Fig. 27. The temperature perturbation contours of the second mode have a so called "rope" like wave structure at the edge of the boundary layer [6]. Figure 27 shows that at the lower figure around the 175 surface station, the wave structure for this frequency is clearly that of the second mode as demonstrated by the rope like wave structure. At the-

earlier surface station around $x/r = 120$, the structure is not the same as that of the second mode. It is shown by the LST analysis in a later section that the stable mode I is dominant in the early region of the boundary layer in the receptivity process.

The profiles of the amplitudes of v perturbations along the wall-normal direction at four surface locations between 46.0 and 175.4 nose radii are shown in Figs. 28 to 31. The figures show the gradual evolution of the wave structure as flow moves from the early region near the leading edge to downstream surface stations. The wave structure at the 175.4 nose radii grid station is similar to that of a second mode. But the wave structures at the earlier stations are those of the stable mode I. We will use LST to identify the wave structures at both the upstream and the downstream stations.

To summarize, the results show a complex development of wave modes induced by freestream acoustic waves. The second mode does not develop in the region where LST predicts unstable second modes to be dominant. Though we are doing further simulations to follow the wave development at further downstream locations, the results that have been obtained so far demonstrate that the second modes are excited at a later location than predicted by the LST analysis. This delay may be caused by the entropy layer effects in the mean flow. The understanding of such receptivity processes may explain the fact that the nose bluntness stablizes hypersonic boundary layer flows. Therefore it is necessary to identify the wave modes in the boundary layer in the receptivity process and to identify the cause of the delay in the development of the second mode waves. The detailed LST analysis results are presented in the following sections.

Boundary-Layer Wave Mode Characteristics

In our previous studies using the linear stability theory, for boundary-layer wave mode characteristics of supersonic flow over a flat plate [17], it was found that the distribution of phase velocities of boundary-layer wave modes is a function of the product of the local Reynolds number (R) and frequency (F). Almost the same distributions of phase velocities *vs* R*F for different boundary-layer wave modes are obtained when F is changed while R is fixed, or when R is changed while F is fixed.

A similar LST study is carried out for hypersonic boundary-layer flow over the blunt cone. Figure 32 shows the spectra of eigenvalues for $w = 0.1934$ at station $s/r = 175$. The relative positions of mode I and the second mode in the spectra are highlighted by circles. When ω increases little by little, the relative positions of mode I and the second mode will gradually change. We can track the position of each mode and obtain their trajectory. The dotted line in Fig. 32 represents the trajectory of mode I when w changes from low to high. It shows that mode I starts from continuous spectra on the left of the spectra, and passes across another continuous spectra in the middle with increasing w. In the same way, we can find the trajectory of the second mode and mode II. Here, mode I and mode II are in fact "multiple-viscous solutions" by Mack [25] and by Eibler and Bestek [26]. The non-dimensional phase velocity of each normal mode can be calculated as

$$a = \frac{\omega}{\alpha_r} . \tag{23}$$

Figure 33 shows phase velocities of three discrete modes, i.e., mode I, mode II and the Mack modes, changing with frequencies at the station $s/r = 175$. The phase velocities of the fast acoustic wave $(1 + 1/M_\infty)$, entropy/vorticity wave (1), and slow acoustic wave $(1 - 1/M_\infty)$ are also shown in the figure for comparison. Both mode I and mode II originate with an initial phase velocity of the fast acoustic wave $(1 + 1/M_\infty)$. Before these two modes become distinct modes, their eigenvalues merge with the continuous spectra. After these two wave modes appear, their phase velocities decrease gradually with increasing w. It's obvious that it is discontinuous for the distributions of phase velocities *vs* w for both mode I and mode II. In Fig. 32, the trajectory of mode I passes across continuous spectra in the middle. In fact, mode I merges with this continuous spectra. Later, another eigenvalue from this continuous spectra becomes discrete mode I. Therefore, there is a gap in the phase velocity curve of mode I. With increasing w, the phase velocity of mode I continues to decrease and passes across the phase velocity curve of Mack modes. At the intersection point ($w = 0.1825$), mode I gets synchronized with the second mode, where both modes have very similar profiles of eigenfunctions. A very similar phenomena happens to mode II at a larger w, which is also shown in Fig. 33.

The growth rates (α_i) of different normal modes are plotted in Fig. 34. While the growth rates of Mack modes are continuous, there are two gaps in the growth rate curves for mode I and mode II. It shows that both mode I and mode II are stable modes. Mack modes are slightly unstable in the range of w between 0.0485 and 0.117. The Mack mode in this range is the conventional first mode. In the range of w between 0.171 and 0.243, the unstable Mack modes are the conventional second mode. In this range, the growth rates of the second mode change dramatically.

Although mode I is stable, it was found that the stable mode I waves play an important role in the receptivity process because they interact with both the forcing acoustic waves and the unstable Mack-mode waves [17]. Through the interactions, the stable mode I waves transfer wave energy from the forcing fast acoustic waves to the second Mack-mode waves.

It should be pointed out that the discontinuous nature of mode I and mode II shown in Fig. 33 is unique to

the current Mach 7.99 flow over a blunt cone. No such phenomena have been observed in our previous studies of supersonic boundary layer over a flat plate [17]. We have also been computing similar stability characteristics of planar 2-D Mach 8 flow over a 5.3° half angle sharp wedge (no nose bluntness). Figure 35 shows the distribution of phase velocities of normal modes with different frequencies for Mach 8 flow over the sharp wedge with the same freestream flow conditions. The figure shows that as w increases, there is no discontinuity in the phase velocity of mode I and mode II when they intersect with the Mack modes. Therefore, it is conjectured that the nose bluntness introduced new characteristics in the wave phase speeds. As shown by Ma and Zhong [17], the excitation of the second mode is a result of the resonant interactions between the mode I and the freestream forcing waves. The induced mode I then interacts with the second mode when they reach the same wave speed and frequency. The discontinuity in the phase velocity in the mode I may lead to no direct interaction of mode I and the second mode. If it is true, there is no excitation of the second mode for the case of blunt cone even when the second mode is predicted by LST to be unstable.

Comparison with LST and Wave Mode Identification

In this section, the linear stability theory is used to identify different wave modes induced by fast acoustic waves. Phase velocities and structures of boundary-layer disturbances from computation of numerical simulations are compared with corresponding values from eigenvalues and eigenfunctions of the linear stability theory at the same frequency. Here, typical frequencies with n = 8, 10 and 15 are chosen for the comparison. The evolution of pressure perturbations on the wall due to freestream disturbances at these three frequencies are redrawn in Fig. 36. At each frequency, the phase velocities of different wave modes are tracked from upstream to downstream by the linear stability theory. The wave structures of mode I at n = 8, the second mode at n = 10 and mode II at $n = 15$ from numerical simulations are compared with those from the linear stability theory at their respective locations.

The phase velocities of the induced boundary-layer disturbances from numerical simulations are calculated based on pressure perturbations on the wall surface by using temporal Fourier analysis according to the following formula:

$$\alpha_r = \frac{d\phi_n}{dx}, \qquad (24)$$

$$(25)$$

where ϕ_n is phase angle at n-th frequency from temporal Fourier analysis. The values calculated by using Eqs. (24) and (23) correspond to the streamwise wave number (α_r) and phase velocity (a) of a single wave if the numerical solutions are dominated by a single discrete wave mode in a local region. If the numerical solutions contain a mixture of two or more wave modes, the values of streamwise wave number and phase velocity demonstrate the result of modulation of these mixed wave modes.

Figure 37 shows the distribution of the phase velocities of boundary-layer disturbances at frequency with $n = 8$ (119.4 kHz) from the simulation. The phase velocities of the Mack modes and modes I from the linear stability theory are also plotted in the same figure for comparison with the numerical solutions. Similar to results shown in Fig. 33, there is a gap in the phase velocity curve of mode I waves from the linear stability theory for the current Mach 7.99 flow over a blunt cone. The figure shows that phase velocities of the induced waves are close to those of mode I waves in the region $x < 66$, which indicates that mode I waves are generated inside the boundary layer in this region. To confirm this conclusion, profiles of induced disturbances in the numerical simulation at $x = 39.3$ are compared with mode I from the linear stability theory. For the purpose of comparison, boundary-layer disturbances are normalized by pressure perturbation on the wall at respective station of comparison. Figures 38 and 39 compare profiles of temperature and velocity disturbances between the linear stability theory and simulation. It shows that the structure of induced disturbances from the numerical simulations matches the structure of mode I wave from the linear stability theory very well. Such agreement also exists in the comparison of other variables, which are not shown here to avoid redundancy. Therefore, the boundary-layer disturbances at this station contain dominant mode I waves.

Figure 40 presents the growth rates of normal modes at frequency with n = 8 from the linear stability theory. It shows that mode I waves are always stable, which is in contradiction with the growth of mode I waves shown in Fig. 36. This contradiction can be explained from the phase velocity curve of mode I shown in Fig. 37. In fact, the phase velocities of mode I waves are very close to those of fast acoustic waves near the leading edge. As a result, mode 1waves are generated near the leading edge region. Though mode I is predicted to be always stable by the linear stability theory, there exists a resonant interaction between mode I waves inside the boundary layer and fast acoustic waves outside the boundary layer in the region upstream. Therefore, mode I waves are strongly amplified before they reach the peak amplitude at $x = 39.3$ (see Fig. 36). The phase velocities of mode I waves decrease during the propagation downstream. When phase velocities of mode I wavea decrease to a certain value and there is no more resonant interaction between mode I waves and acoustic waves, mode I waves decay due to their inherent stable properties after they reach the peak amplitude at $x = 39.3$. With the decay of mode I waves, modulation between mode I waves

with acoustic waves and other waves leads to the oscillation in phase velocities in downstream, which is also shown in Fig. 37. At the beginning, this kind of oscillation is around the phase velocities of mode I, when the component of mode I waves included in boundary-layer disturbances is relatively strong. In the region downstream ($x > 150$), this kind of oscillation is around the phase velocity of fast acoustic waves, which indicates the relative dominance of fast acoustic waves included in boundary-layer disturbances.

A similar analysis is carried out for the frequency with $n = 10$ (149.2 kHz). Figure 41 compares phase velocities of boundary-layer disturbances at frequency with $n = 10$ from the simulation with the phase velocities of the Mack modes and modes I from the linear stability theory. Again, in the region upstream ($x < 36$), the phase velocities of boundary-layer disturbances induced by fast acoustic waves are close to those of mode I waves from the linear stability theory in upstream region. In addition, it was found (not shown here) that the structure of boundary-layer disturbances from the simulation can match those of mode I waves from the linear stability theory. There is strong oscillation in phase velocity curve due to the modulation between mode I waves and other waves, such as fast acoustic waves, after mode I waves are no longer dominant in the region with $x > 36$. Due to the stable property of mode I waves, the amplitude of mode I waves gradually decay when mode I waves propagate downstream. Before they die out, mode I waves get synchronized with the second Mack mode. The synchronization point between mode I and the second mode at a frequency with n = 10 is located at $w = 0.1808$ ($x = 117.28$), which is very close to that shown in Fig. 33 with $w = 0.1825$ at the station $s/r = 175$ (or $x = 172$). At the synchronization point, both mode I and the second Mack mode have very similar profiles of eigenfunctions. As a result, mode I waves convert to the second-mode waves.

The growth rates of boundary-layer normal modes at frequency with n = 10 from the linear stability theory are shown in Fig. 42. Again, it shows that mode I waves are always stable. For Mack modes, the second-mode Branch I neutral point is located at $x = 97.47$. They become unstable in the region after $x > 97.47$. In addition, the growth rates of the second-mode waves reach peak value $\alpha_i = -0.00452$ at $x = 142.54$. In other words, the second mode is most unstable and should be strongly amplified at this location. However, there are no amplified second-mode waves at frequency with $n = 10$ shown in Fig. 36 between $x = 90$ and $x = 115$. On the contrary, the amplitude of boundary-layer disturbances gradually decays at this frequency. This can be explained from phase velocity curves shown in Fig. 41. The second-mode waves are converted from mode 1 waves at the synchronization point between mode I and the second mode, which is located at $x = 117.28$. Therefore, the second-mode waves only appear after $x = 117.28$ in this case. This is the reason why there are no amplified second-mode waves at frequency with $n = 10$ shown in Fig. 36 between $x = 90$ and $x = 115$. After the generation of the second-mode waves, the boundary-layer disturbances are strongly amplified resulting from the unstable property of the second mode in the downstream region $x > 117.28$, which is obviously shown in Fig. 36. The structures of induced second-mode waves at $x = 177$ are compared with the eigenfunctions of the second mode from the linear stability theory, which are shown in Fig. 43 for temperature and 44 for streamwise velocity, respectively. Again, there is good agreement in wave structure of the second mode between the numerical simulation and the linear stability theory. The visible difference in the comparison is because there are other wave components, such as fast acoustic waves, included in the boundary-layer disturbances besides the second-mode waves from the numerical simulation.

At frequency with n = 15, the LST results of growth rates in Fig. 45 show that all normal modes are stable. The stable property of the second mode at this frequency is in agreement with the LST results of Malik *et* al.[10]. The phase velocities of boundary-layer disturbances at frequency with n = 15 from the simulation are compared with the phase velocities of the Mack modes, modes I and mode II from the linear stability theory, which is plotted in Fig. 46. Once again, it shows that mode I waves are generated and amplified due to the resonant interaction between mode I waves and fast acoustic waves in the region upstream ($x < 9.5$), where the structure of boundary-layer disturbances from the simulation can match those of mode I waves from the linear stability theory. The modulation between mode I waves and other waves, such as fast acoustic waves, lead to strong oscillations in the phase velocity curve during the decay of mode I waves. Because the second mode is stable, there is no amplified second mode at frequency with n = 15 shown in Fig. 36. However, there is another wave mode which is strongly amplified during propagation downstream after $x > 50$. Figure 46 shows that this wave mode is mode 11. Although mode II waves are predicted to be stable by the linear stability theory, they are strongly amplified due to the resonant interaction between mode II waves and fast acoustic waves because their phase velocities are very close to each other. The structures of mode II waves at $x = 149$ from numerical Simulation are compared with those from the linear stability theory at the same location, which is presented in Fig. 47 and 48. There is very good agreement in the comparison except visible difference outside the boundary layer due to acoustic waves in the simulation.

To summarize the LST analysis of the simulation results, it is clear that the synchronization location between mode I and the second mode plays an important role in the receptivity of the second Mack mode in the

boundary layer. In the current flow over a blunt cone, the synchronization location is located downstream of the branch I neutral stability location of the second mode. As a result, there are no noticeable second mode components in the region before the synchronization location even though the second is linearly unstable there. Therefore mode I plays a very important role in the receptivity process. In addition, the current flow over a blunt cone also has a discontinuous phase velocity as the waves propagate downstream. Such discontinuities in the phase velocity curves may also contribute to the lack of second mode excitation. These factors lead to much lower levels of second mode excitation in hypersonic boundary layers over a blunt cone.

CASE II. $T' = 0$ BOUNDARY CONDITION

As discussed earlier, the receptivity using the zero temperature perturbation boundary condition is also simulated for the same flow conditions as Case I. Again, the steady base flow has an adiabatic wall, but the temperature disturbances have a $T' = 0$ boundary condition. Again, the unsteady flow solutions are obtained by imposing freestream disturbances according to Table 1 and Eq. (6), containing 15 frequencies. The results show that the wave fields of Case I and Case II are very similar with the delayed development of the second mode. Therefore, only the main results are presented here.

Figure 49 shows the development of wave amplitudes of pressure perturbations in the boundary layer as functions of x/r. The figure shows the development of wave modes induced by the freestream forcing waves. Again, there is no apparent presence of the unstable second mode in the main computational region. In order to see the development of wave amplitudes of each frequency more clearly, the wave amplitude spectra for surface pressure perturbations obtained by the numerical simulation are shown in Fig. 50 for the 88.3 surface station. This figure shows that the unstable second mode is not apparent in the numerical solutions.

Similar to Case I, in order to examine the development of the wave modes for the case of 149.2 kHz more clearly, Fig. 51 shows the amplitudes of pressure perturbations along the cone surface for this frequency. The figure shows there are wave modulation of multiple waves as the waves propagate downstream along the surface. The wave amplitudes decrease along the surface as the wave propagates downstream. It is expected that the second mode will be generated further downstream. Again, the excitation of the second mode does not coincide with the beginning of the unstable region predicted by LST. The development of the wave modes can also be seen from the temperature disturbance contours shown in Fig. 52. At this early surface station around $x/r = 90$, the structure is not that of the second mode, but that of stable mode I.

CASE III. SURFACE BLOWING AND SUCTION

One possible explanation for the delay of the development of the second mode by freestream acoustic waves is that the receptivity of the second mode is altered, or suppressed, by the entropy layer effects in the blunt cone flow field. In this section we demonstrate that the unstable second mode can develop in the boundary layer once it is excited in the region predicted by LST to be unstable. One way to directly excite the second mode wave is to use surface blowing and suction in a narrow surface region upstream of the second mode region.

Therefore, we conduct the simulation of Case III with no freestream disturbances, but with surface blowing and suction in a small region near the $z/s = 105$ station. There is no clearly dominant second mode in the case of freestream acoustic waves. The amplitudes of the forcing waves are determined by the parameter ϵ in Eq. (11) with the same 15 frequencies shown in Table 1. The dominant second mode waves observed by experiments and also predicted by the linear stability analysis is around 140 kHz. The relative nondimensional amplitudes of these amplitudes are chosen to be the same by setting A_n to 1, while their phase angles ϕ_n are randomly chosen. For the results presented in this paper, $\epsilon = 0.0005$, which produces pressure perturbation at the blowing and suction strip at the level of approximately 3.8% of the pressure behind the shock at the same grid station.

Simulation Results

Figure 53 shows the distribution of the pressure perturbation amplitudes for 15 fundamental frequencies (shown in Table 1) along the body surface. This figure shows the development of the second mode induced by surface blowing and suction. The figure shows that at the end of the blowing and suction region, the frequency of 149.2 kHz show the strongest growth. This frequency is consistent with the LST prediction.

The total perturbations of the flow variables in the unsteady flow field is a combination of all wave modes developed in the boundary layer. Figures 54 show the contours for the instantaneous temperature and pressure perturbations for the most unstable 149.2 kHz frequency ($n = 10$) after the flow field reaches a time periodic state. The instantaneous contours show the development of typical second mode instability waves in the boundary layer on the surface. The shape of the second-mode waves at the edge demonstrate the shape of the "rope-like" waves observed in experiments [27]. Figure 55 shows the contours for the instantaneous perturbation p' of 149.2 kHz. In addition to the typical second-mode wave developing in the boundary layer, there are also some components of acoustic Mach waves outside of the boundary layer. These acoustic waves are induced at the blowing and suction strip and propagate along

the Mach lines in the flow field. Again, the waves are dominated by the most amplified second mode waves in the boundary layer.

Figure 56 shows the frequency spectra of surface pressure perturbation amplitudes at the 130.9 surface locations downstream of the blowing and suction strip. The figures show that the wave amplitudes of different frequencies. The amplitudes of fundamental mode n = 10 at 149.2 kHz are most amplified.

The profiles of the amplitudes of v perturbations along the wall-normal direction at the surface location of 130.9 nose radii in Fig. 57. The figure shows the wave structure of a second mode in the boundary layer.

Comparison with LST and Wave Mode Identification

According to our previous studies [28], very clean second-mode waves can be obtained by blowing and suction from the wall. From Fig. 53, the boundary-layer disturbances at frequency with n = 10 are most amplified, so this frequency is picked out to compare with the LST analysis.

The phase velocities and growth rates of the induced boundary-layer disturbances at frequency with $n = 10$ at 149.2 kHz from numerical simulations are calculated based on pressure perturbations on the wall surface by using temporal Fourier analysis. Figure 58 compares the phase velocities of the induced boundary-layer disturbances from blowing and suction with those of the second mode from the linear stability theory. There is good agreement in the region with $x > 120$. The difference in the region with $x < 120$ is due to the effect of initial transient of the forcing waves from blowing and suction.

The growth rates of the induced second mode from blowing and suction is also compared with that from the linear stability theory, which is shown in Fig. 59. There is a large difference in the growth rates obtained from the simulation results and LST results. Further studies will be required to explain this difference. However, there is very good agreement in the comparison of the second-mode structures between the simulation results and LST results, as shown in Figs. 60 and 61.

SUMMARY AND CONCLUSIONS

In this paper, we have studied the receptivity of Mach 8 flow over a 7° half-angle blunt cone, corresponding to Stetson's experiments. Both the steady base flow solutions and three cases of unsteady flow solutions have been obtained and studied. The main conclusions are:

1. The current steady flow solutions agree very well with those computed by Esfanhanian and Herbert [11] and compare well with experimental results on surface pressures and tangential velocities out side of the boundary layer. The mean flow solutions also demonstrate the effects of the entropy layer on the steady flow field.

2. The receptivity of the Stetson's Mach 7.99 flow over the blunt cone to freestream fast acoustic waves is simulated by solving the full Navier-Stokes equations. The simulation results show a complex development of wave modes induced by freestream acoustic waves. The second mode does not develop in the region where LST predicts dominant unstable second modes. The second modes are excited at a later location than predicted by the LST analysis. This delay is unique for the current flow over a blunt cone. It may be caused by the entropy layer effects in the mean flow. The understanding of such receptivity processes may explain the fact that the nose bluntness stablizes hypersonic boundary layer flows. Therefore the results of LST calculations are used to identify the wave modes in the boundary layer in the receptivity process and to study the cause of the delay of the development of the second mode waves.

3. The wave structures obtained from the simulations are compared with those obtained from the LST for mode I, mode II, and the second mode. Very good agreement was obtained. The wave modes induced by the freestream acoustic waves are mode I near the nose, as it propagate downstream, second mode or mode II are excited due to the mechanism of resonant interactions between different wave modes.

4. The LST analysis shows that the synchronization location between mode I and the second mode plays an important role in the receptivity of the second Mack mode in the boundary layer. In the current flow over a blunt cone, the synchronization location is located downstream of the branch I neutral stability location of the second mode. As a results, there are no noticeable second mode components in the region before the synchronization location even though the second mode is linearly unstable there. Therefore mode I plays a very important role in the receptivity process, and leads to the lack of excitation of the second mode in the current flow over a blunt cone.

5. In addition, the current flow over a blunt cone also has a discontinuous phase velocity as the waves propagate downstream. Such discontinuities in the phase velocity curves may also contribute to the lack of second mode excitation. These factors lead to the much lower levels of second mode excitations in hypersonic boundary layers over a blunt cone. On the other hand, our previous studies on Mach 4.5 flow over a flat plate and Mach 8 flow over a sharp wedge show do not show similar characteristics of the mode I structure and the second mode is strongly excited by the freestream waves.

6. When the disturbances are excited by surface blowing-and-suction, the second mode waves are generated directly. The wave mode structures agree very well with those of the second mode predicted by LST. However, the growth rate predicted by LST is much larger than those obtained by numerical simulations.

7. Further and more extensive parametric studies are currently under way by the authors to study the receptivity mechanisms in the blunt cone flow fields. The most important aspects of future studies include: receptivity to freestream slow acoustic waves and other types of waves, 3-D wave effects, wall temperature effects, and nonlinear effects, etc.

ACKNOWLEDGMENTS

This work was sponsored by the Air Force Office of Scientific Research, USAF, under AFOSR Grant #F49620-00-1-0101, monitored by Dr. John Schmisseur. The views and conclusions contained herein are those of the author and should not be interpreted as necessarily representing the official policies or endorsements either expressed or implied, of the Air Force Office of Scientific Research or the U.S. Government.

References

[1] Mack, L. M., "Boundary Layer Linear Stability Theory," *AGARD report, No. 709,* 1984, pp. 3–1 to 3–81.

[2] Arnal, D., "Laminar-Turbulent Transition Problems In Supersonic and Hypersonic Flows," *Special Course on Aerothermodynamics of Hypersonic Vehicles,* Vol. AGARD Report No. 761, 1988.

[3] Stetson, K. F. and Kimmel, R. L., "On Hypersonic Boundary Layer Stability," *AIAA paper 92-0737,* 1992.

[4] Stetson, K. F., Thompson, E. R., Donaldson, J. C., and Siler, L. G., "Laminar Boundary Layer Stability Experiments on a Cone at Mach 8, Part 2: Blunt Cone," *AZAA* paper *84-0006,* January 1984.

[5] Schneider, S. P., "Hypersonic Laminar Instability on Round Cones Near Zero Angle of Attack," *AIAA Paper 2001-0206,* 2001.

[6] Demetriades, A., "Hypersonic Viscous Flow Over A Slander Cone. Part 111: Laminar Instability and Transition," *AIAA* paper *74-535,* 1974.

[7] Demetriades, A., "Laminar Boundary Layer Stability Measurements at Mach 7 Including Wall Temperature Effects," *AFOSR-TR-77-1511,* Vol. November, 1977.

[8] Maslov, A. A., Shiplyuk, A. N., Sidorenko, A., and Arnal, D., "Leading-edge receptivity of a hypersonic boundary layer on a flat plate," *Jounml of Fluid Mechanics,* Vol. 426, 2001, pp. 73–94.

[9] Maslov, A. A., Mironov, S. G., and Shiplyuk, A. A., "Hypersonic Flow Stability Experiments," *AIAA Paper 2002-0153,2002.*

[10] Malik, M. R., Spall, R. E., and Chang, C.-L., "Effect of Nose Bluntness on Boundary Layer Stability and Transition," *AZAA paper 90-0112,* 1990.

[11] Herbert, T. and Esfahanian, V., "Stability of Hypersonic Flow over a Blunt Body," AGARD *CP-514,* Vol. pp. 28-1 – 12, April, 1993.

[12] Kufner, E., Dallmann, U., and Stilla, J., "Instability of Hypersonic Flow Past Blunt Cones – Effects of Mean Flow Variations," *AZAA paper 93-2989,* June 1993.

[13] Kufner, E. and Dallmaun, U., "Entropy- and Boundary Layer Instability of Hypersonic Cone Flows – Effects of Mean Flow Variations," *IUTAM Symposium on Laminar-Turbulent Transition,* Vol. Sendai/Japan, September 1994, pp. 197-204, Springer-Verlag, Berlin, 1994.

[14] Reshotko, E., "Hypersonic Stability and Transition," *in Hypersonic* Flows *for Reentry Problems, Eds. J.-A. Desideri, R. Glowinski, and J. Periaux, Springer-Verlag,* Vol. 1, 1991, pp. 18–34.

[15] Morkovin, M. V., "Transition at Hypersonic Speeds," *ICASE Interim Report 1,* Vol. NASA CR 178315, May, 1987.

[16] Zhong, X., "Leading-Edge Receptivity to Free Stream Disturbance Waves for Hypersonic Flow Over A Parabola," *Journal of Fluid Mechanics,* Vol. 441,2001, pp. 315–367.

[17] Ma, Y. and Zhong, X., "Receptivity to Freestream Disturbances of Mach 4.5 Flow over a Flat Plate," *AZAA paper 2002-0140,* 2002.

[18] Zhong, X., "Direct Numerical Simulation of Hypersonic Boundary-Layer Transition Over Blunt Leading Edges, Part 11: Receptivity to Sound (Invited)," *AIAA paper 97-0756,* January 1997.

[19] Zhong, X. and Tatineni, M., "Stable High-Order Schemes and DNS of Boundary-Layer Stability on a Blunt Cone at Mach 8," *AIAA Paper 2001-0437,* 2001.

[20] Zhong, X., "Direct Numerical Simulation of Hypersonic Boundary-Layer Transition Over Blunt Leading Edges, Part I: New Numerical Methods and Validation (Invited)," *AZAA puper 97-0755,*

35th AZAA Aerospace Sciences Meeting and Exhibit, January 6-9, Reno, Nevada, 1997.

[21] Zhong, X., "High-Order Finite-Difference Schemes for Numerical Simulation of Hypersonic Boundary-Layer Transition," *Journal* of *Computational Physics*, Vol. 144, August 1998, pp. 662–709.

[22] Esfahanian, V., *Computation and stability analysis of laminar flow* over *a blunt cone in* hypersonic *flow*, Ph.D. thesis, The Ohio State University, 1991.

[23] Malik, M. R., "Numerical Methods for Hypersonic Boundary Layer Stability," *Journal of Comp. Phys.*, Vol. 86, 1990, pp. 376–413.

[24] Lees, L. and Lin, C. C., "Investigation of the Stability of the Laminar Boundary Layer in Compressible Fluid," *NACA TN No. 1115,* 1946.

[25] Mack, L. M., "Stability of Axisymmetric Boundary Layers on Sharp Cones at Hypersonic Mach Numbers," *AIAA Paper 87-1413,* 1987.

[26] Eibler, W. and Bestek, H., "Spatial Numerical Simulations of Linear and Weakly Nonlinear Instabilities in Supersonic Boundary Layers," *Theoretical and Computational Fluid Dynamics,* Vol. 8, 1996, pp. 219–235.

[27] Stetson, K. F. and Kimmel, R., "On the Breakdown of a Hypersonic Laminar Boundary Layer," *AIAA Paper 93-0896*, 1993.

[28] Ma, Y. and Zhong, X., "Numerical Simulation of Receptivity and Stability of Nonequilibrium Reacting Hypersonic Boundary Layers ," *AZAA* paper *2001-0892,* 2001.

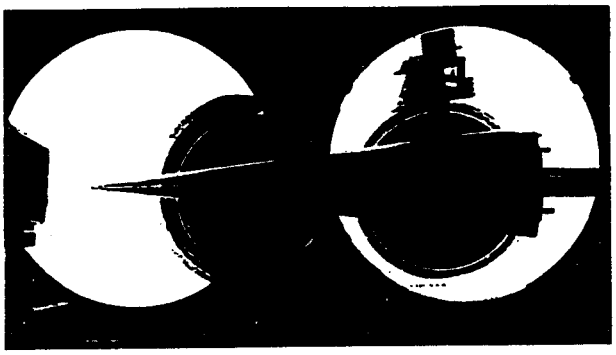

Figure 1: The 7° blunt cone of Stetson's (1984) Mach 7.99 stability experiment.

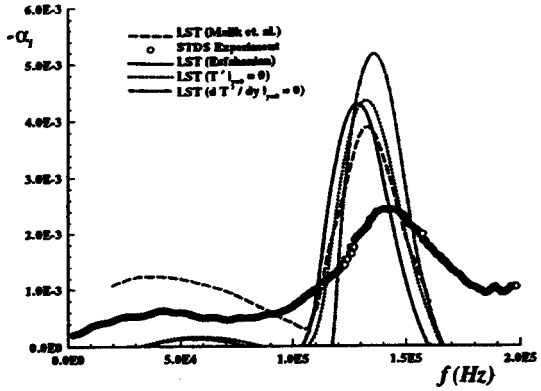

Figure 4: Comparison of disturbance growth rates predicted by LST and experiments at $s/r = 175$ ($x/r = 172$).

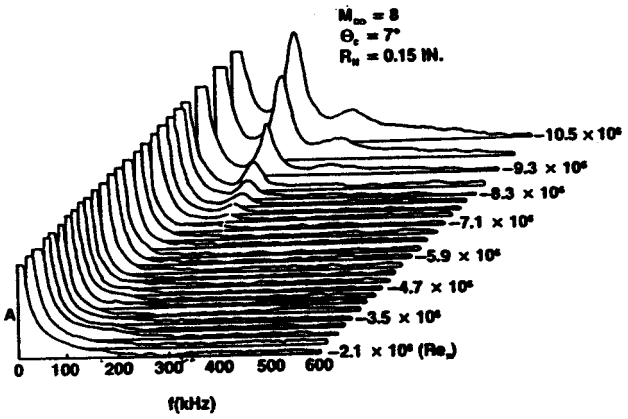

Figure 2: Experimental fluctuation spectra along the cone surface obtained by Stetson et al. (1984), where $s/r = Re_s/3.35 \times 10^4$.

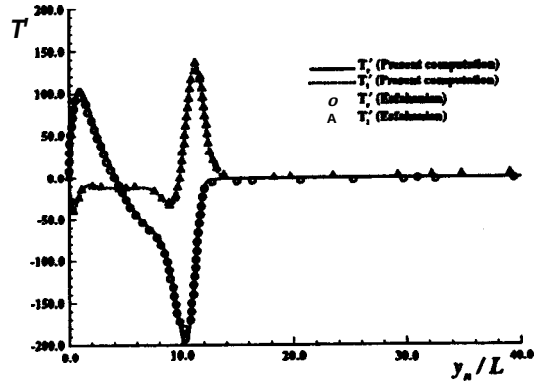

Figure 5: Comparison of the second mode T' eigenfunctions from LST with $s/r = 175, \omega = 0.1934$ (127.56 kHz).

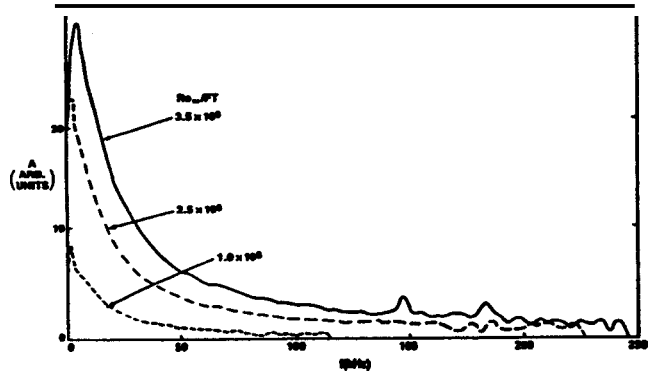

Figure 3: Freestream disturbance spectra in Stetson et al.'s experiments (1984).

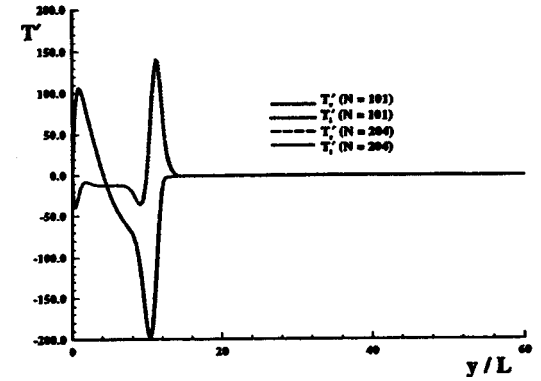

Figure 6: The second **mode T' eigenfunctions** from LST using two sets of grids with $s/r = 175, \omega = 0.1934$ (127.56 kHz).

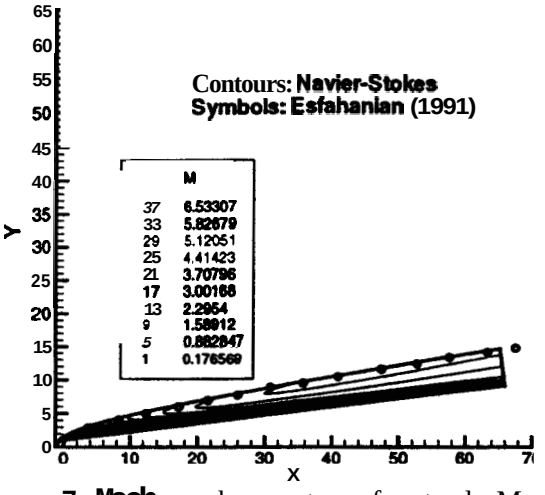

Figure 7: Mach number contours for steady Mach 7.99 flow with an adiabatic wall.

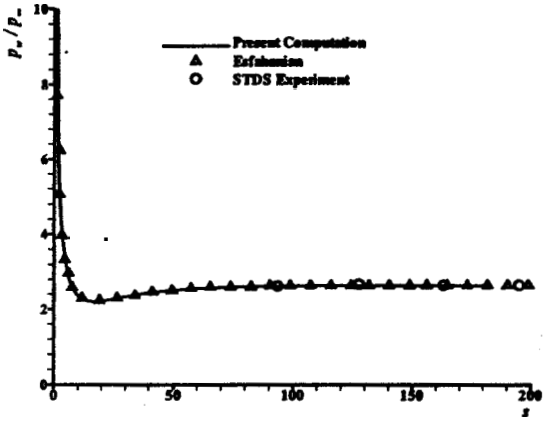

Figure 8: Steady pressure along the cone surface.

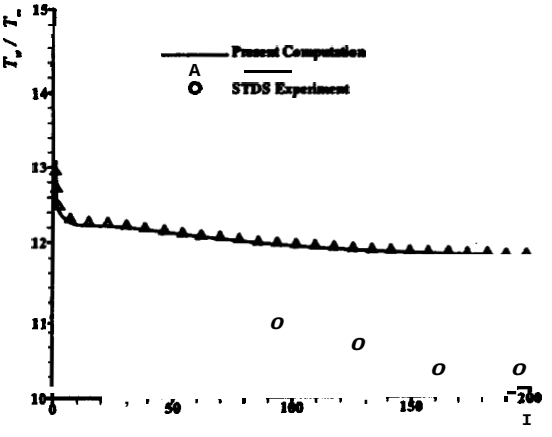

Figure 9: Steady temperature along the cone surface.

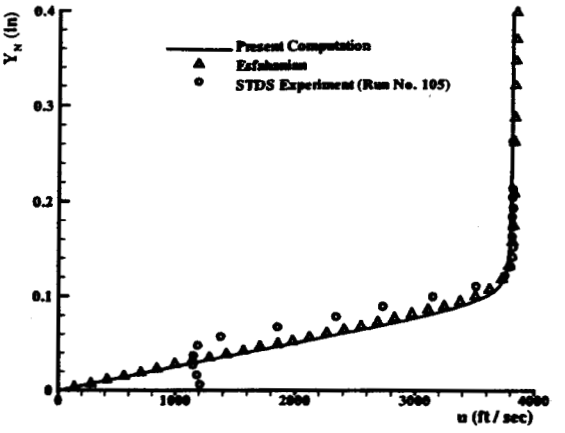

Figure 10: Steady tangential velocity profiles along the wall-normal direction at the surface location of 94 nose radii.

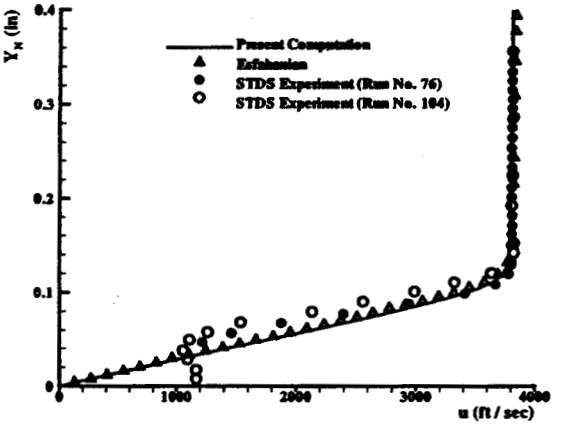

Figure 11: Steady tangential velocity profiles along the wall-normal direction at the surface location of 128 nose radii.

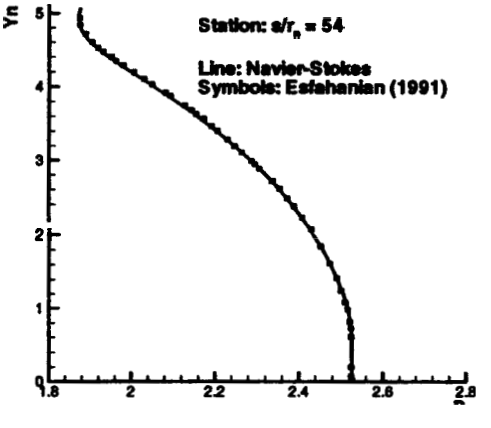

Figure 12: Pressure profiles at station $s/r_n = 54$. The results are compared with those of Esfahanian and Herbert (1991).

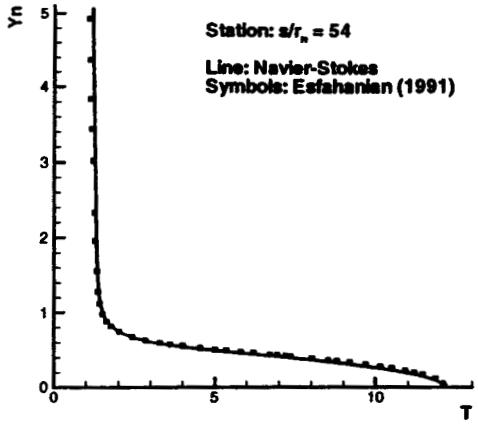

Figure 13: Temperature profiles at station $s/r = 54$. The results are compared with those of Esfahanian and Herbert (1991).

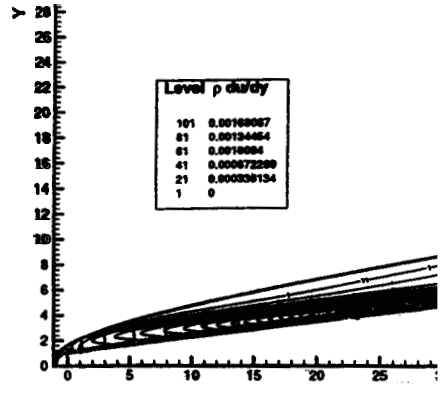

Figure 16: Contours of $\rho \frac{du_t}{dy_n}$, which is affected by the entropy layer.

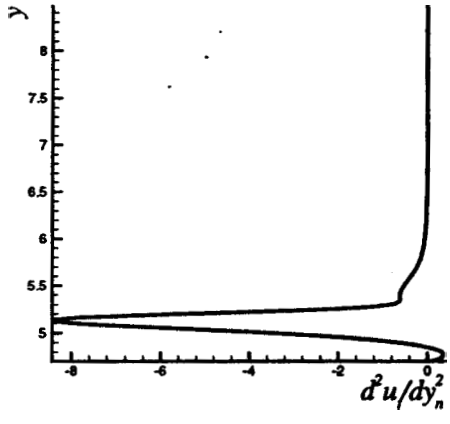

Figure 14: Second derivative of steady tangential velocity profiles along the wall-normal direction at the surface location of 31.9 nose radii.

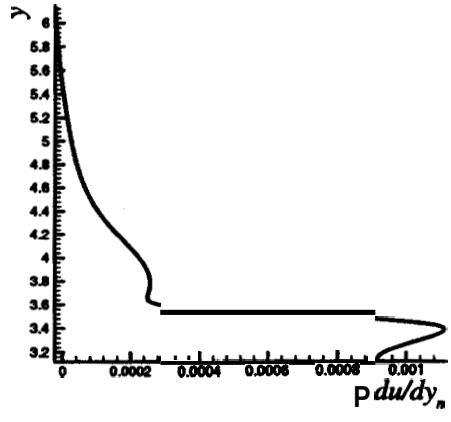

Figure 17: The profile of $\rho \frac{du_t}{dy_n}$ along the wall-normal direction at the surface location of 18.9 nose radii.

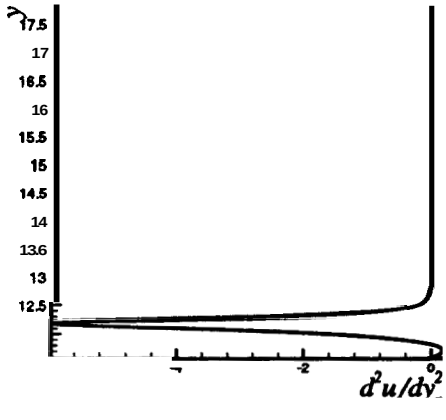

Figure 15: Second derivative of steady tangential velocity profiles along the wall-normal direction at the surface location of 88.3 nose radii.

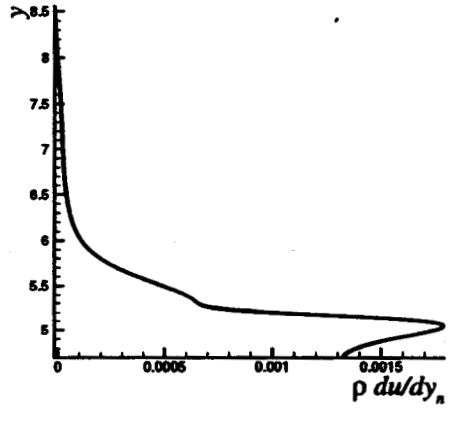

Figure 18: The profile of $\rho \frac{du_t}{dy_n}$ along the wall-normal direction at the surface location of 31.9 nose radii.

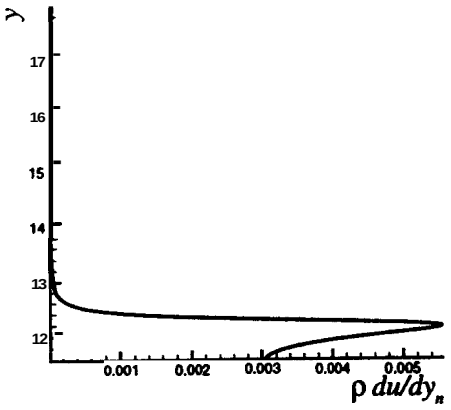

Figure 19: The profile of $\rho\frac{du_t}{dy_n}$ along the wall-normal direction at the surface location of 88.3 nose radii.

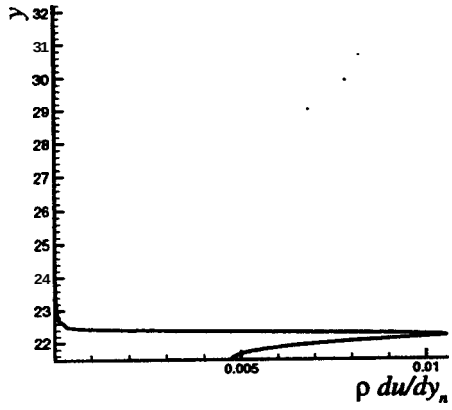

Figure 20: The profile of $\rho\frac{du_t}{dy_n}$ along the wall-normal direction at the surface location of 169.4 nose radii.

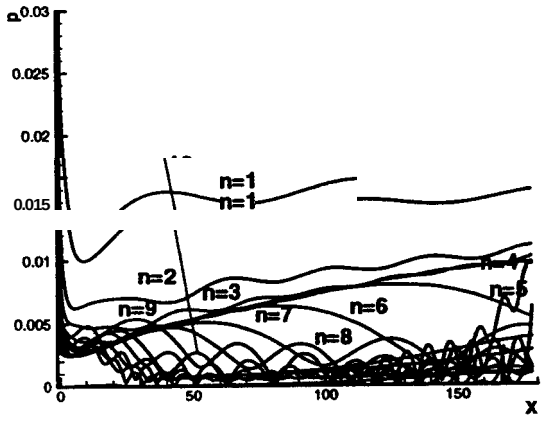

Figure 21: Amplitudes of pressure perturbations on the cone surface vs. x/r. The lines represent 15 different frequencies of $f = nf_1$, where $f_1^* = 14.922kHz$ and $n = 1, 2, \cdots, 15$.

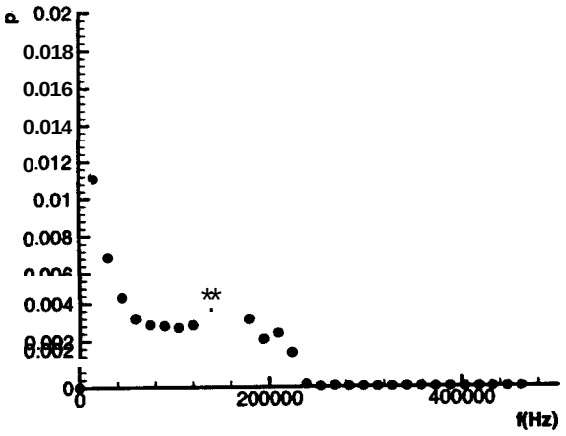

Figure 22: The frequency spectrum of the pressure perturbations on the cone surface at the surface location of 18.9 nose radii.

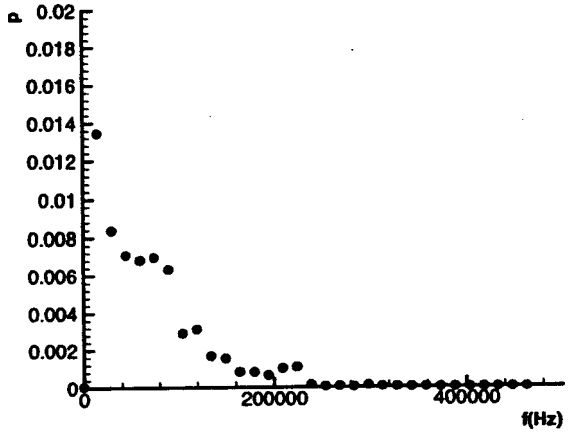

Figure 23: The frequency spectrum of the pressure perturbations on the cone surface at the surface location of 88.3 nose radii.

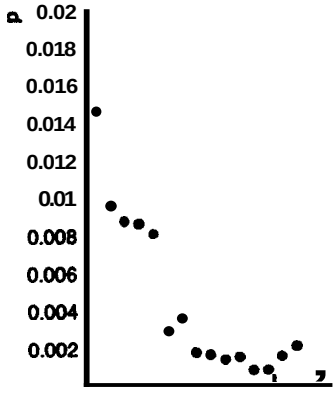

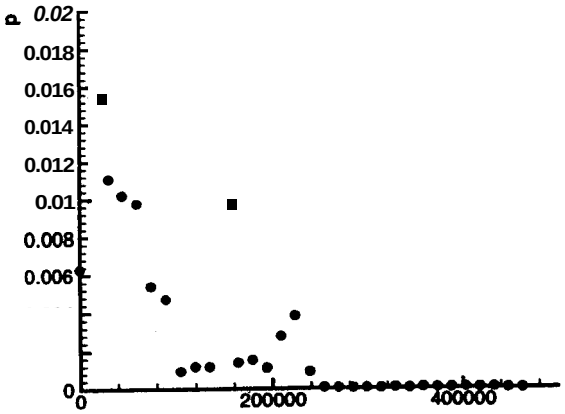

Figure 25: The frequency spectrum of the pressure perturbations on the cone surface at the surface location of 175.4 nose radii.

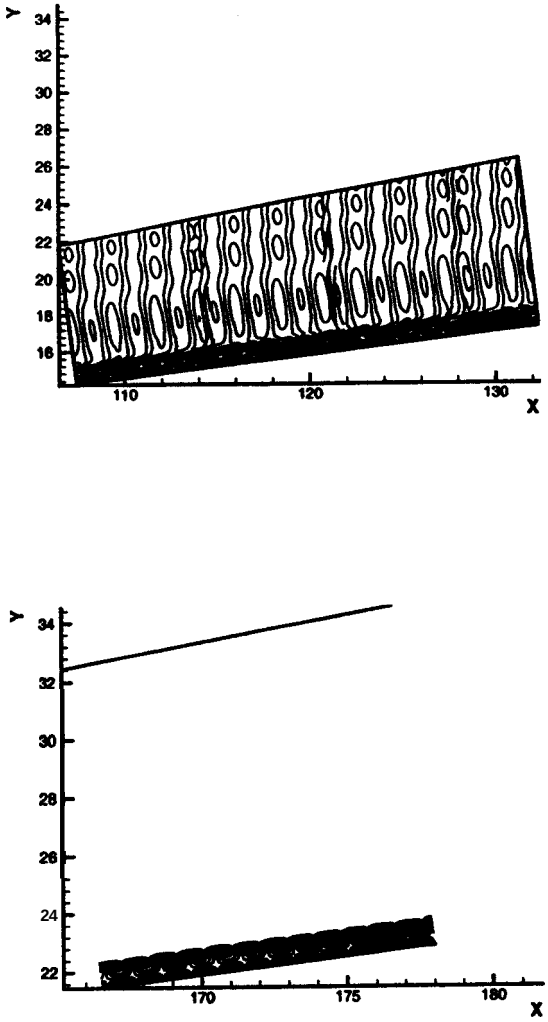

Figure 27: Contours of real part of temperature perturbation in two sections of the flow field for the frequency of $f^* = 149.2kHz$ (n = 10)

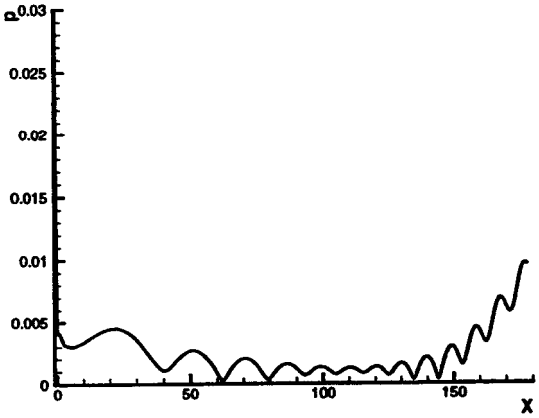

Figure 26: Amplitudes of pressure perturbations on the cone surface vs. x/r for the frequency of $f^* = 149.2kHz$ $(n = 10)$.

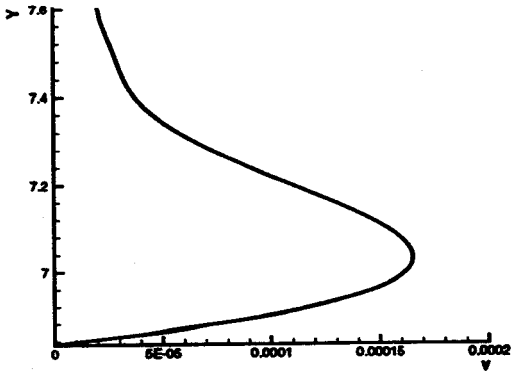

Figure 28: Profile of the amplitudes of v perturbations along the wall-normal direction at the surface location of 46.0 nose radii.

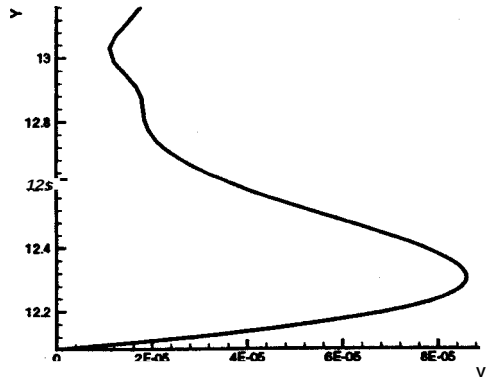

Figure 29: Profile of the amplitudes of v perturbations along the wall-normal direction at the surface location of 88.3 nose radii.

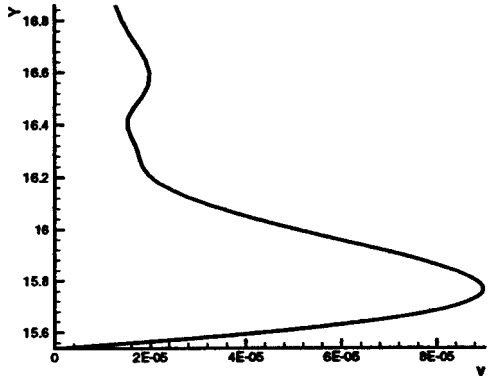

Figure 30: Profile of the amplitudes of v perturbations along the wall-normal direction at the surface location of 130.9 nose radii.

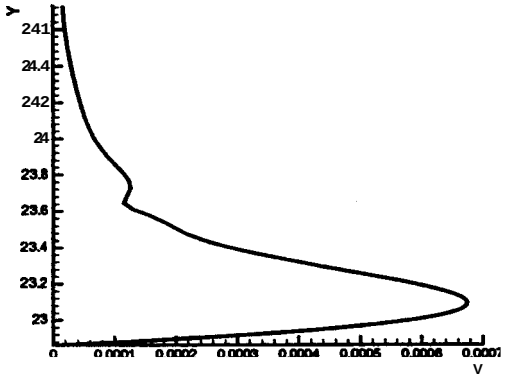

Figure 31: Profile of $|v'|$ along the wall-normal direction ($s/r = 175.4$).

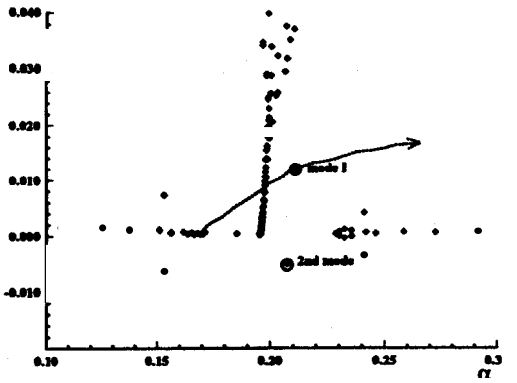

Figure 32: Spectra of eigenvalues with $w = 0.1934$ (127.56 kHz), $s/r = 175$ ($x/r = 172$) and trajectory of mode I when the values of w increase.

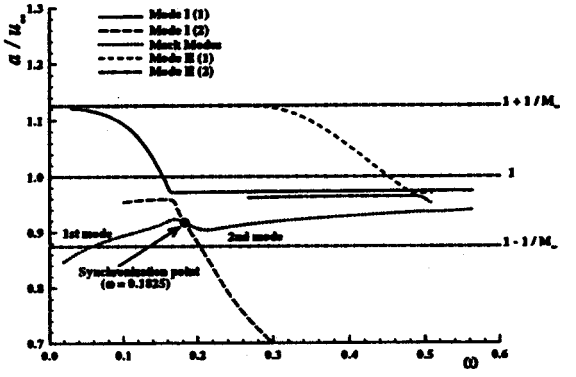

Figure 33: The distribution of phase velocities of normal modes with different frequencies at the station $s/r = 170$.

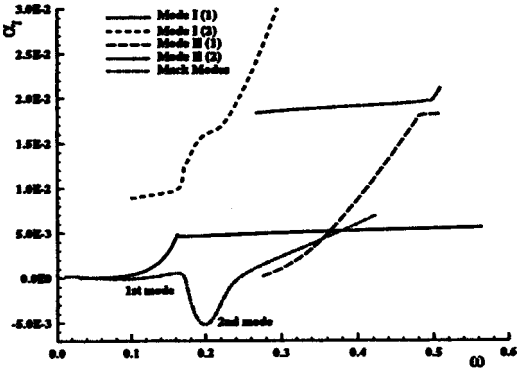

Figure 34: The distribution of growth rates of normal modes with different frequencies at the station $s/r = 175$.

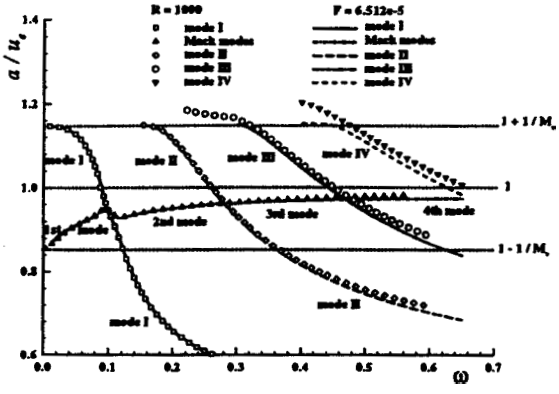

Figure 35: The distribution of phase velocities of normal modes with different frequencies for Mach 8 flow over 5.3° half angle sharp wedge with the same freestream flow conditions.

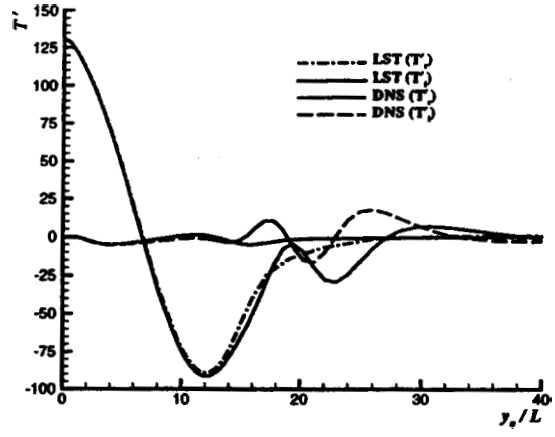

Figure 38: Comparison of wave structures with T eigenfunctions of mode I from the LST with $n = 8$, $x = 39.3$.

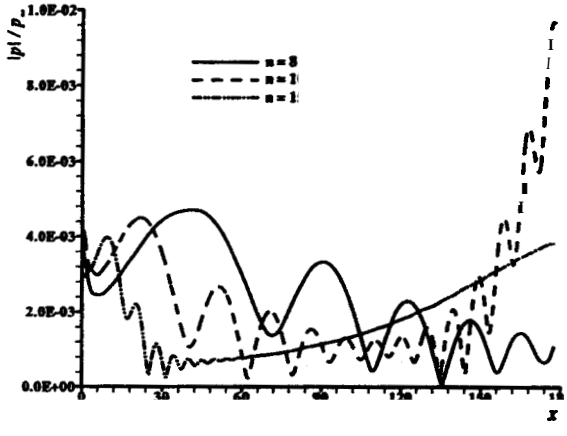

Figure 36: Amplitudes of pressure perturbations on the cone surface vs. x/r at frequencies with $n = 8, 10, 15$.

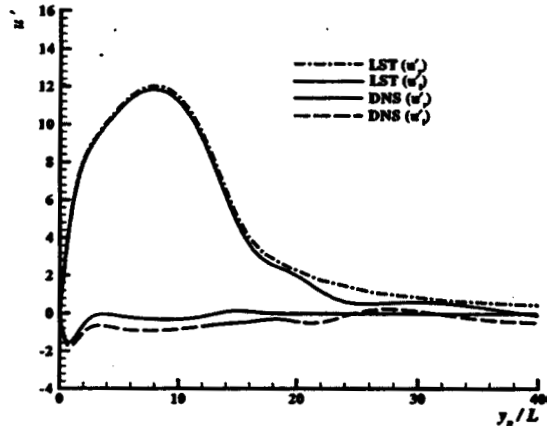

Figure 39: Comparison of wave structures with u eigenfunctions of mode I from the LST with $n = 8$, $x = 39.3$.

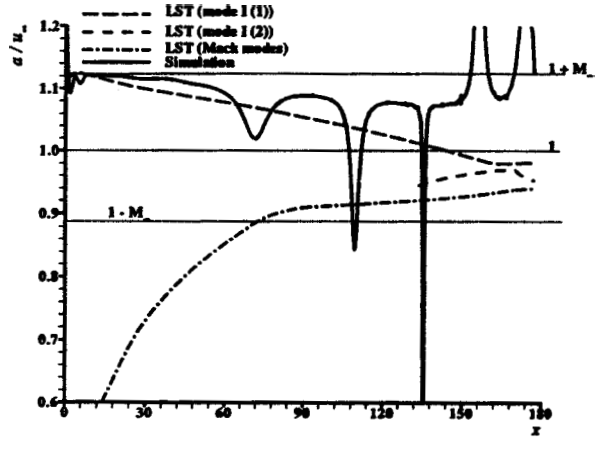

Figure 37: Comparison of phase velocities on the cone surface with phase velocities of boundary-layer normal modes at frequencies with $n = 8$.

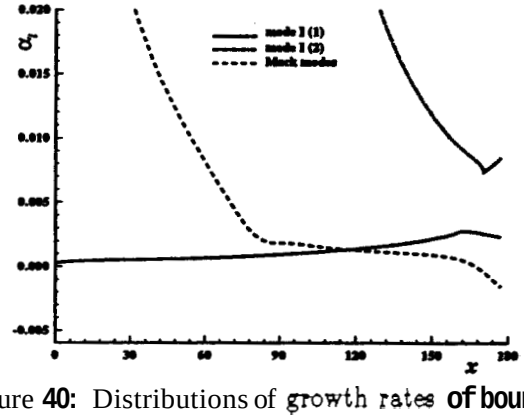

Figure 40: Distributions of growth rates of boundary-layer normal modes with $n = 8$.

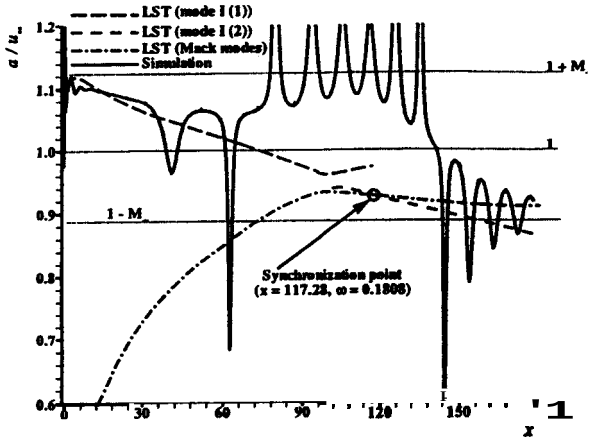

Figure 41: Comparison of phase velocities on the cone surface with phase velocities of boundary-layer normal modes at frequencies with $n = 10$.

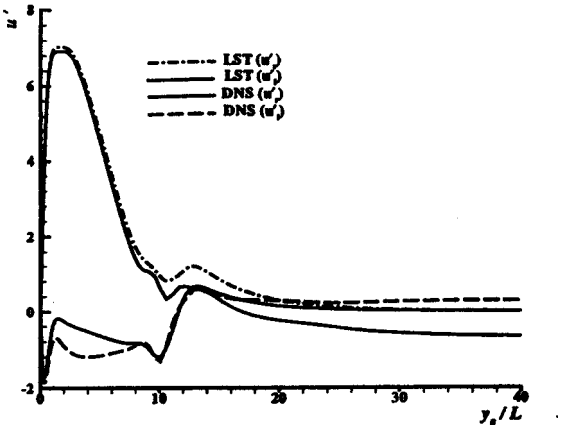

Figure 44: Comparison of wave structures with u eigenfunctions of the second mode from the LST with $n = 10$, $x = 177$.

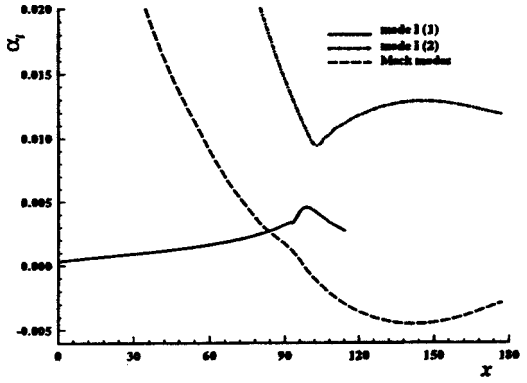

Figure 42: Distributions of growth rates of boundary-layer normal modes with $n = 10$.

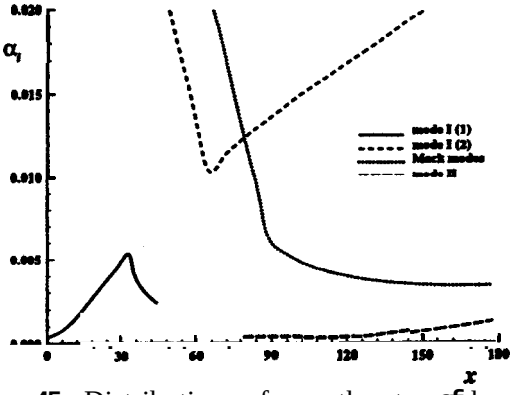

Figure 45: Distributions of growth rates of boundary-layer normal modes with $n = 15$.

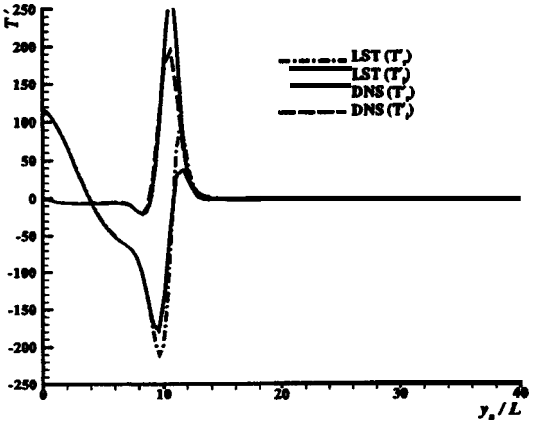

Figure 43: Cornparison of wave structures with T eigenfunctions of the second mode from the LST with $n = 10$, $x = 177$.

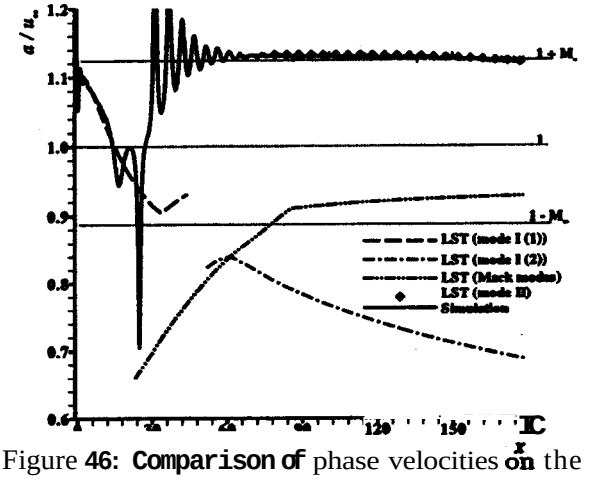

Figure 46: Comparison of phase velocities on the cone surface with phase velocities of boundary-layer normal modes at frequencies with $n = 15$.

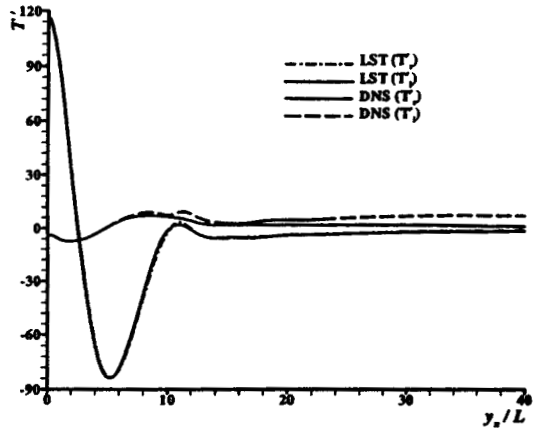

Figure 47: Comparison of wave structures with T eigenfunctions of mode II from the LST with n = 15, x = 149.

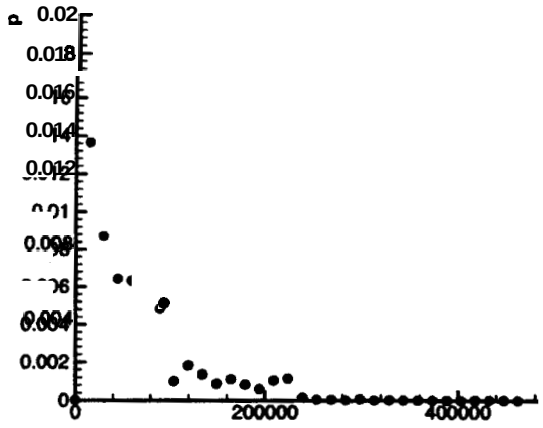

Figure 50: Frequency spectrum of the surface pressure perturbations (s/r = 88.3), for the case of isothermal disturbance boundary condition.

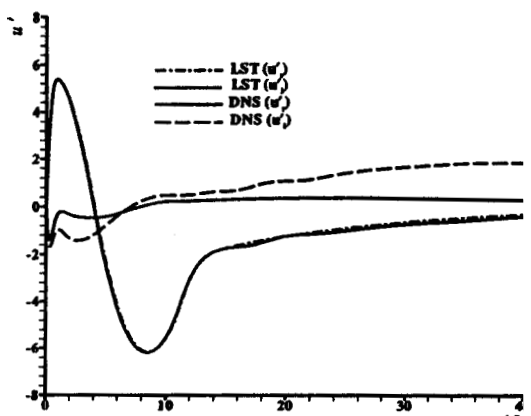

Figure 48: Comparison of wave structures with u eigenfunctions of the second mode from the LST with n = 15, x = 149.

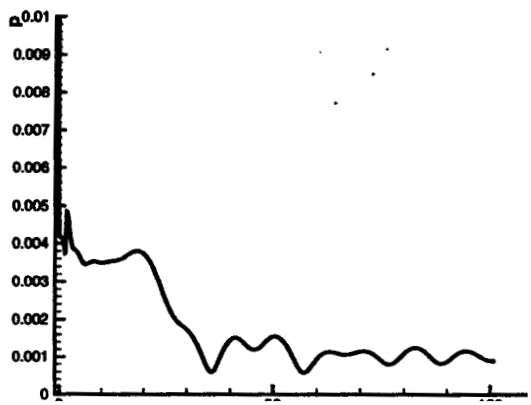

Figure 51: Amplitudes of surface pressure perturbations vs. x/r (f' = 149.2kHz, n = 10) for the case of isothermal disturbance boundary condition.

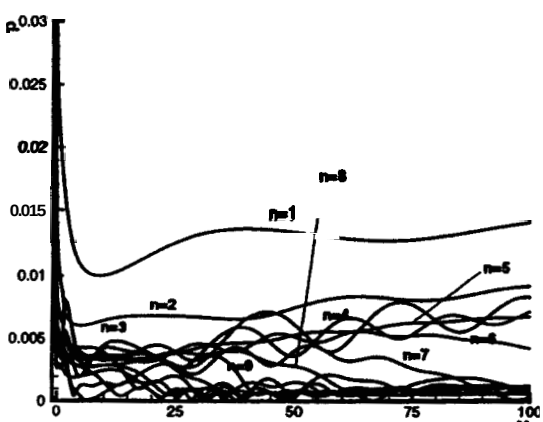

Figure 49: Amplitudes of surface pressure perturbations vs. x/r for the case of isothermal disturbance boundary condition.

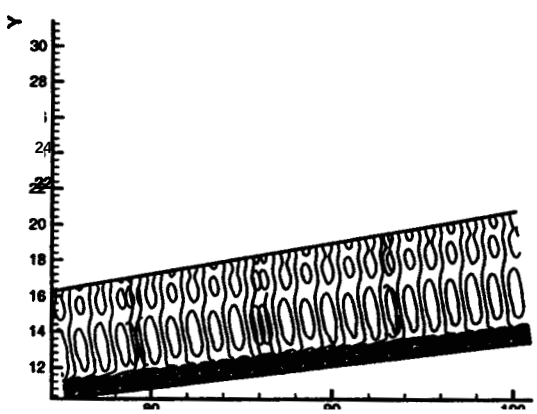

Figure 52: Contours of real part of temperature perturbations (f' = 149.2kHz, n = 10) for the case of isothermal disturbance boundary condition.

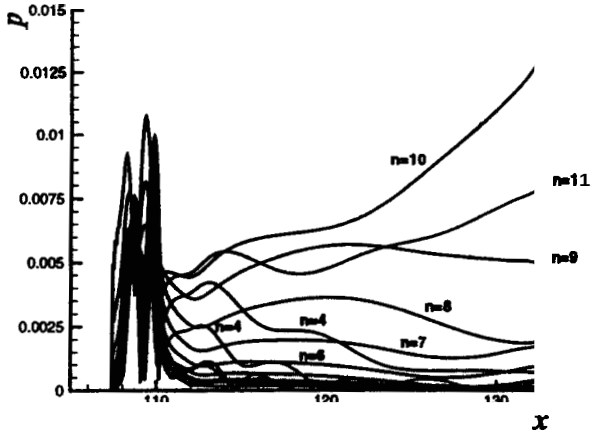

Figure 53: Amplitudes of surface pressure perturbations vs. x/r for the case of blowing-and-suction. The lines represent 15 different frequencies of $f = nf_1$.

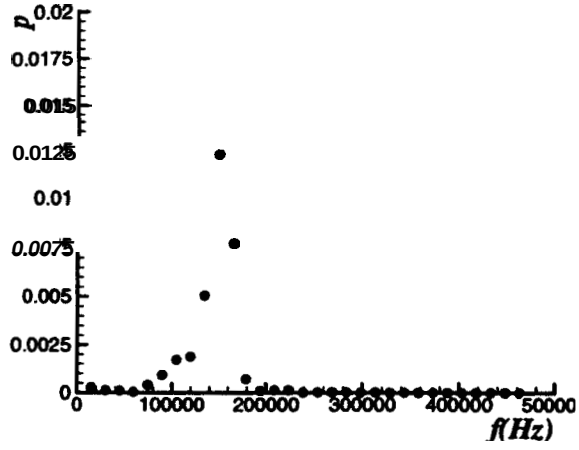

Figure 56: Frequency spectrum of the pressure perturbations on the cone surface ($s/r = 130.9$) for the blowing-and-suction case.

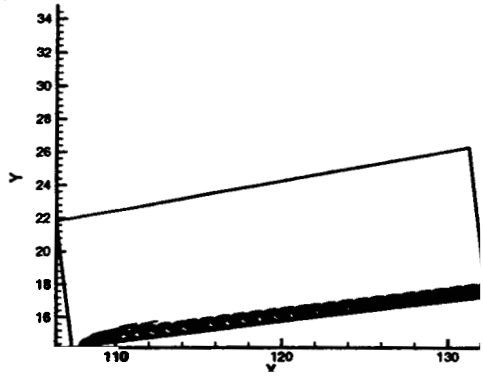

Figure 54: Contours of real part of temperature perturbation ($f^* = 149.2kHz$, $n = 10$) for the case of blowing-and-suction.

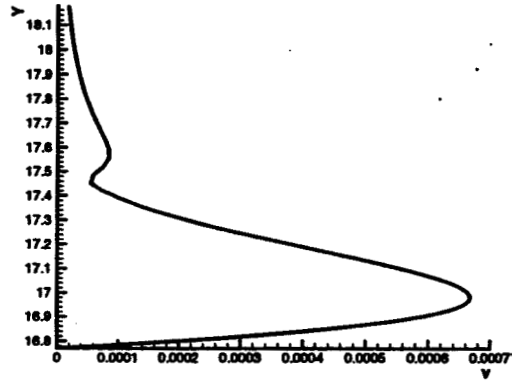

Figure 57: Profile of v perturbation amplitudes along the wall-normal direction ($s/r = 130.9, n = 10$) for the blowing-and-suction case.

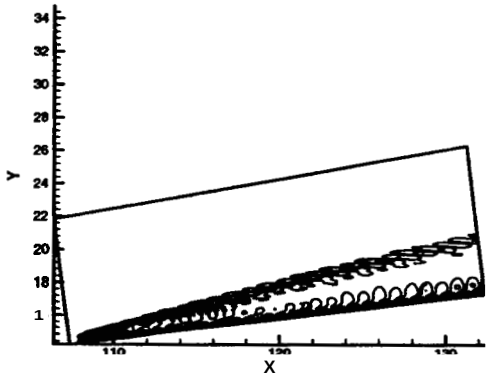

Figure 55: Contours of real part of pressure perturbation in a section of the flow field ($f^* = 149.2kHz$, $n = 10$) for the blowing-and-suction case.

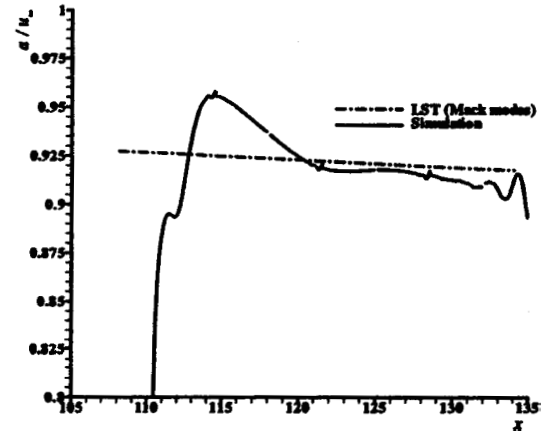

Figure 58: Comparison of phase velocities on the cone surface with phase velocities of the second mode at frequency with $n = 10$.

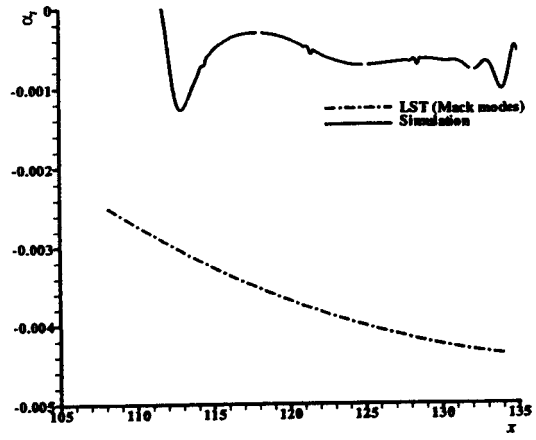

Figure 59: Comparison of growth rates of the second mode at frequency with n = 10.

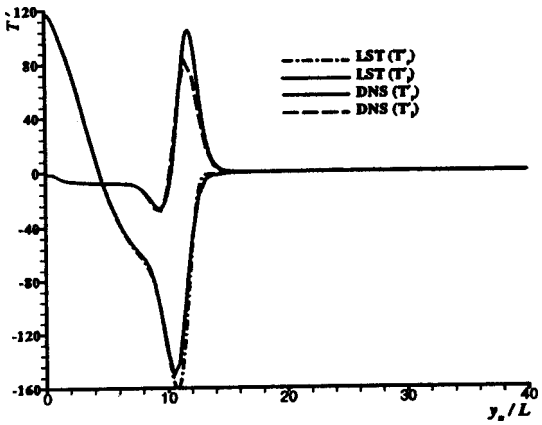

Figure 60: Comparison of wave structures with T eigenfunctions of the second mode from the LST with n = 10, x = 130.

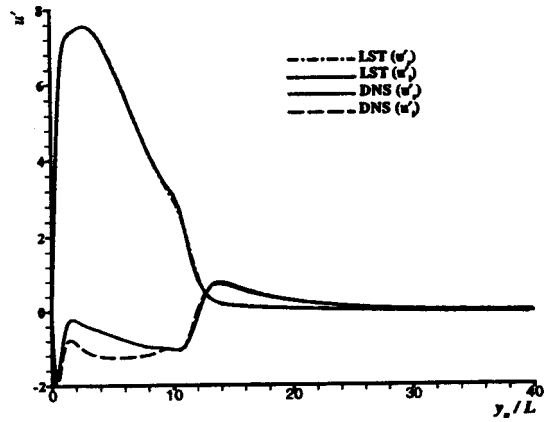

Figure 61: Comparison of wave structures with u eigenfunctions of the second mode from the LST with n = 10, x = 130.